Structure of crystalline and amorphous materials in the NASICON system Na$_{1+x}$Al$_x$Ge$_{2-x}$(PO$_4$)$_3$ (F)

(iD) **Lawrence V. D. Gammond,** (iD) **Henry Auer,** (iD) **Rita Mendes Da Silva,** (iD) **Anita Zeidler,** (iD) **Jairo F. Ortiz-Mosquera,** (iD) **Adriana M. Nieto-Muñoz,** (iD) **Ana Candida M. Rodrigues,** (iD) **Igor d'Anciães Almeida Silva,** (iD) **Hellmut Eckert,** **Chris J. Benmore,** and (iD) **Philip S. Salmon**

COLLECTIONS

(F)   This paper was selected as Featured

Structure of crystalline and amorphous materials in the NASICON system $Na_{1+x}Al_xGe_{2-x}(PO_4)_3$ Ⓕ

View Online   Export Citation   CrossMark

Lawrence V. D. Gammond,[1] ⓘD   Henry Auer,[2] ⓘD   Rita Mendes Da Silva,[1] ⓘD   Anita Zeidler,[1] ⓘD
Jairo F. Ortiz-Mosquera,[3] ⓘD   Adriana M. Nieto-Muñoz,[3] ⓘD   Ana Candida M. Rodrigues,[4] ⓘD
Igor d'Anciães Almeida Silva,[5] ⓘD   Hellmut Eckert,[5,6]   Chris J. Benmore,[7] ⓘD   and Philip S. Salmon[1,a) ⓘD

AFFILIATIONS

[1] Department of Physics, University of Bath, Bath BA2 7AY, United Kingdom
[2] Fraunhofer Institute for Ceramic Technologies and Systems IKTS, Winterbergstraße 28, 01277 Dresden, Germany
[3] Universidade Federal de São Carlos, Programa de Pós-Graduação em Ciência e Engenharia de Materiais, CP 676,
  13565-905 São Carlos, SP, Brazil
[4] Departamento de Engenharia de Materiais, Universidade Federal de São Carlos, CP 676, 13565-905 São Carlos, SP, Brazil
[5] Instituto de Física de São Carlos, Universidade de São Paulo, CP 369, São Carlos SP 13566-590, SP, Brazil
[6] Institut für Physikalische Chemie, WWU Münster, Corrensstraße 30, D48149 Münster, Germany
[7] X-ray Science Division, Advanced Photon Source, Argonne National Laboratory, 9700 South Cass Avenue, Lemont,
  Illinois 60439, USA

a)Author to whom correspondence should be addressed: p.s.salmon@bath.ac.uk

ABSTRACT

The structure of crystalline and amorphous materials in the sodium (Na) super-ionic conductor system $Na_{1+x}Al_xGe_{2-x}(PO_4)_3$ with $x = 0$, 0.4, and 0.8 was investigated by combining (i) neutron and x-ray powder diffraction and pair-distribution function analysis with (ii) ^{27}Al and ^{31}P magic angle spinning (MAS) and $^{31}P/^{23}Na$ double-resonance nuclear magnetic resonance (NMR) spectroscopy. A Rietveld analysis of the powder diffraction patterns shows that the $x = 0$ and $x = 0.4$ compositions crystallize into space group-type $R\bar{3}$, whereas the $x = 0.8$ composition crystallizes into space group-type $R\bar{3}c$. For the as-prepared glass, the pair-distribution functions and ^{27}Al MAS NMR spectra show the formation of sub-octahedral Ge and Al centered units, which leads to the creation of non-bridging oxygen (NBO) atoms. The influence of these atoms on the ion mobility is discussed. When the as-prepared glass is relaxed by thermal annealing, there is an increase in the Ge and Al coordination numbers that leads to a decrease in the fraction of NBO atoms. A model is proposed for the $x = 0$ glass in which super-structural units containing octahedral $Ge^{(6)}$ and tetrahedral $P^{(3)}$ motifs are embedded in a matrix of tetrahedral $Ge^{(4)}$ units, where superscripts denote the number of bridging oxygen atoms. The super-structural units can grow in size by a reaction in which NBO atoms on the $P^{(3)}$ motifs are used to convert $Ge^{(4)}$ to $Ge^{(6)}$ units. The resultant $P^{(4)}$ motifs thereby provide the nucleation sites for crystal growth via a homogeneous nucleation mechanism.

Published under an exclusive license by AIP Publishing. https://doi.org/10.1063/5.0049399

I. INTRODUCTION

Homogeneous (or internal) nucleation in bulk glass can be used to create a uniform distribution of crystallites of controllable size and shape throughout a material. This process is crucial in the production of many glass-ceramics that include photosensitive and photochromic materials, along with tough fracture-resistant ceramics that have uses ranging from cookware to missile nose-cones.[1] The creation of a uniform distribution of

crystallites also makes homogeneous nucleation an attractive option for optimizing the properties of superionic conducting materials for battery and sensor applications. A case example is provided by the technologically relevant $Na_{1+x}Al_xGe_{2-x}(PO_4)_3$ ($0 \leq x \leq 1$) (NAGP) system in which the structure of the crystalline phase is based on that of the sodium (Na) super-ionic conductor (NASICON) $NaGe_2(PO_4)_3$.[2]

Initial work on these highly conducting materials, which are candidates for the electrolyte in all-solid-state sodium ion

batteries,[3,4] focused on pressed powders. However, it was discovered that they can also be prepared via the glass-ceramic route, giving the significant advantage of moldable bulk materials.[5] It is therefore desirable to know the glass structure and how this structure changes during thermal annealing and the early stages of crystal nucleation and growth. The latter is of general scientific interest for any glass undergoing homogeneous nucleation but has not been explored in non-siliceous systems.[6]

In this paper, we investigate the structure of NAGP materials with $x = 0$, 0.4, and 0.8. Here, the structure of the crystalline phase with $x = 0$ is based on a negatively charged three-dimensional framework in which tetrahedral PO_4 units are linked via bridging oxygen (BO) atoms to four octahedral GeO_6 units. This framework of corner-sharing polyhedra contains interstitial sites in which the Na^+ ions reside[2] and where the size of a connection between sites determines the extent to which it acts as a bottleneck for ion motion.[7] The ionic conductivity increases when a proportion of the Ge^{4+} ions are aliovalently substituted by Al^{3+} ions, and additional Na^+ ions enter interstitial sites to compensate for the charge deficit.[8] For glassy NAGP materials, the ionic conductivity also increases with x, and the addition of Al improves the glass-forming ability.[8] The lithium analogs $Li_{1+x}Al_xGe_{2-x}(PO_4)_3$ (LAGP) of these materials nucleate homogeneously[9] and have already found commercial usage as separator membranes in lithium–air batteries and related systems.[3,10] Comparatively little is known, however, about the Na-containing materials, although solid-state nuclear magnetic resonance (NMR) experiments on the LAGP[11] and NAGP[12] systems indicate that all structural aspects of the glass-to-crystal transition are the same, suggesting the same crystallization mechanisms. Homogeneous nucleation in NAGP glasses is supported by the results obtained from differential scanning calorimetry experiments on monolithic vs powdered samples.[8]

The structure of the NAGP materials was probed by combining neutron diffraction (ND) and x-ray diffraction (XRD) with ^{27}Al and ^{31}P magic angle spinning (MAS) and ^{31}P/^{23}Na double-resonance NMR spectroscopy. The structure of the glass was investigated in its as-prepared condition and after thermal annealing near the glass-transition temperature T_g in order to investigate the initial stages of thermal relaxation. The structure of the fully crystallized glass was also investigated by applying (i) the Rietveld method[13,14] to refine powder diffraction patterns and (ii) the pair-distribution function method. The results for the crystalline materials provided a starting point for interpreting the pair-distribution functions measured for the vitreous materials. Here, the analysis was helped by the provision of site-specific information on the coordination environments of P and Al from the solid-state NMR experiments. In turn, the pair-distribution functions provided information on the Ge coordination environment, which is largely inaccessible from NMR spectroscopy.

This paper is organized as follows. The diffraction theory for pair-distribution function analysis is outlined in Sec. II, and the experimental methods are described in Sec. III. The results are presented in Sec. IV and are discussed in Sec. V where a model is proposed for the glass structure. Conclusions are drawn in Sec. VI.

II. THEORY FOR PAIR-DISTRIBUTION FUNCTIONS

In a diffraction experiment, the total structure factor[15]

$$S(k) = 1 + \frac{1}{\langle w(k) \rangle^2} \sum_\alpha \sum_\beta c_\alpha c_\beta w_\alpha(k) w_\beta(k) [S_{\alpha\beta}(k) - 1] \quad (1)$$

is measured, where k denotes the magnitude of the scattering vector; $c_\alpha \equiv N_\alpha/N$ denotes the atomic fraction of chemical species α, where N_α is the number of atoms of type α and $N = \sum_\alpha N_\alpha$ is the total number of atoms; $w_\alpha(k)$ represents the k-dependent x-ray atomic form-factor $f_\alpha(k)$ or the k-independent coherent neutron scattering length b_α of chemical species α; the mean value $\langle w(k) \rangle = \sum_\alpha c_\alpha w_\alpha(k)$; and $S_{\alpha\beta}(k)$ is a Faber–Ziman partial structure factor. Neutral atom form-factors were used in the XRD data analysis.[16] The neutron scattering lengths of the elements in NAGP materials are $b_{Na} = 3.63(2)$ fm, $b_{Al} = 3.449(5)$ fm, $b_{Ge} = 8.185(20)$ fm, $b_P = 5.13(1)$ fm, and $b_O = 5.803(4)$ fm.[17]

The corresponding real-space information can be represented by the total pair-distribution function

$$D'(r) = \frac{2}{\pi} \int_0^\infty dk\, k[S(k) - 1]M(k)\sin(kr)$$
$$= D(r) \otimes M(r), \quad (2)$$

where r is a distance in real space and $\otimes$ denotes the one-dimensional convolution operator. $M(k)$ is a window function that originates from the finite k-range that is accessible to a diffractometer, which extends to a maximum value k_{max}. This accessibility has the effect of applying to $S(k) - 1$ the step modification function defined by $M(k) = 1$ for $k \le k_{max}$ and $M(k) = 0$ for $k > k_{max}$. $M(r)$ is the real-space manifestation of $M(k)$ and is a symmetrical function. In a neutron diffraction experiment, where the scattering lengths are k independent,

$$D(r) = \frac{4\pi\rho\, r}{\langle b \rangle^2} \sum_\alpha \sum_\beta c_\alpha c_\beta b_\alpha b_\beta [g_{\alpha\beta}(r) - 1], \quad (3)$$

where ρ is the atomic number density and $g_{\alpha\beta}(r)$ is a partial pair-distribution function. At r-values smaller than the distance of the closest approach between two atoms, $g_{\alpha\beta}(r) = 0$. It follows that, in the absence of Fourier transform artifacts, such as those originating from $M(k)$, $D'(r) = -4\pi\rho r$, which is often called the density line.

In order to distinguish between features in $D'(r)$ that describe the glass structure from those that are an artifact of $M(r)$, each peak i in $rg_{\alpha\beta}(r)$ can be represented by the Gaussian function

$$p_{\alpha\beta}^i(r) = \frac{1}{4\pi\rho} \frac{\bar{n}_\alpha^\beta(i)}{c_\beta^i r_{\alpha\beta}^i} \frac{1}{\sqrt{2\pi}\sigma_{\alpha\beta}^i} \exp\left[-\frac{(r - r_{\alpha\beta}^i)^2}{2(\sigma_{\alpha\beta}^i)^2}\right], \quad (4)$$

where $r_{\alpha\beta}^i$, $\sigma_{\alpha\beta}^i$, and $\bar{n}_\alpha^\beta(i)$ are the peak position, standard deviation, and coordination number of chemical species β around α, respectively.[18] The contribution of each peak $p_{\alpha\beta}^i(r)$ to $S(k) - 1$ is given by

$$p_{\alpha\beta}^i(k) = W_{\alpha\beta}^i \frac{\bar{n}_\alpha^\beta(i)}{c_\beta^i} \frac{\sin(k r_{\alpha\beta}^i)}{k r_{\alpha\beta}^i} \exp\left[-\frac{k^2(\sigma_{\alpha\beta}^i)^2}{2}\right], \quad (5)$$

where $W_{\alpha\beta}^i = (2 - \delta_{\alpha\beta})c_\alpha^i c_\beta^i w_\alpha^i(k) w_\beta^i(k)/\langle w(k) \rangle^2$ and $\delta_{\alpha\beta}$ is the Kronecker delta.

In the case of the ND data, the method of least squares was used to fit $D'(r)$ to a sum of Gaussian functions convoluted with $M(r)$ such that

$$D'(r) = 4\pi\rho \sum_i W_{\alpha\beta}^i p_{\alpha\beta}^i(r) \otimes M(r) - 4\pi\rho r. \quad (6)$$

In the case of the XRD data, each $p_{\alpha\beta}^i(k)$ function was Fourier transformed to real-space using the same $M(k)$ function as used for the experimental data. For a selected region in r-space, the method of least squares was then used to fit an appropriate sum of these Fourier transforms to $T'(r) = T(r) \otimes M(r)$ using the program PXFIT (Hannon, private communication), where $T(r) \equiv D(r) + T^0(r)$ and $T^0(r) = 4\pi\rho r$. For ease of comparison with the neutron diffraction results, the fitted functions are presented as $D'(r) = [T(r) - T^0(r)] \otimes M(r) = T'(r) - 4\pi\rho r$, noting that $T^0(r) \otimes M(r) = T^0(r)$ because $M(k = 0) = 1$. The goodness-of-fit was assessed by the parameter[19]

$$R_\chi = \left\{ \frac{\sum_j [D_{exp}(r_j) - D_{fit}(r_j)]^2}{\sum_j D_{exp}^2(r_j)} \right\}^{1/2}, \quad (7)$$

calculated over the fitted range, where "exp" and "fit" denote the measured and fitted functions, respectively.

The use of a step modification function in Eq. (2) not only leads to sharp peaks in $D'(r)$, which is the reason for its application, but can also lead to Fourier transform artifacts that include large excursions below the density line $D'(r) = -4\pi\rho r$ on each side of the first peak in $D'(r)$. The latter can be suppressed by using the Lorch[20,21] modification function $M(k) = \sin(\pi k/k_{max})/(\pi k/k_{max})$ for $k \leq k_{max}$ and $M(k) = 0$ for $k > k_{max}$, but at the expense of broadened peaks.

III. EXPERIMENT

A. Sample preparation and characterization

The glasses were made using the method described in Ref. 8. For each composition, part of the glass was kept in its as-prepared condition, part was annealed at a thermal treatment temperature T_{TT} near to T_g for a time chosen to relax the glass structure while minimizing the formation of crystallites, and part was annealed at T_{TT} for a time chosen to fully crystallize the material. For the $x = 0$ composition, two additional parts of the as-prepared glass were taken for further investigation. One part was annealed at $T_{TT} = 876$ K for 0.25 h, and the other part was annealed at the same temperature for 0.5 h.

The glass transition temperature T_g and crystallization temperature T_x were measured for ~20 mg monolithic samples using a differential scanning calorimeter (Netzsch DSC404) with a heating rate of 10 K/min. The mass density of the glasses was measured using a Quantachrome 1200e pycnometer operated with He gas. The density of the crystals was taken from the powder diffraction work. Parameters describing the samples and their thermal history are listed in Table I.

B. Powder diffraction experiments

The neutron powder diffraction patterns were measured using the fine resolution powder diffractometer E9 (FIREPOD)[22] at the reactor source BER II, Helmholtz-Zentrum Berlin (HZB), Germany. The datasets were collected at ambient temperature (295 K) using an incident wavelength $\lambda = 1.7982(1)$ Å. The samples were handled in air and held in vanadium cans of 5 mm diameter. The x-ray powder diffraction patterns were measured using a Rigaku Smart-Lab system with Bragg–Brentano diffraction geometry, monochromatic copper Kα_1 radiation, and a fixed $0.66°$ divergence slit. The instrument was equipped with a Johansson-type Ge-crystal monochromator and a HyPix-3000 2D single photon counting detector.

Rietveld refinement[13,14] of the crystal structures was performed using the FullProf suite.[23,24] The ND and XRD patterns for each sample were refined simultaneously. The crystal structure data were standardized using STRUCTURE TIDY.[25] Crystal structures were drawn using the three-dimensional visualization system for electronic and structural analysis (VESTA) package, version 3.3.1.[26]

C. Pair-distribution function experiments

Two sets of ND experiments were performed on the NAGP materials to measure the total pair-distribution functions.

The first set of experiments used the D4c diffractometer at the Institut Laue–Langevin[27] with $\lambda = 0.4955(1)$ Å (for the samples annealed at $T_{TT} = 876$ K) or $\lambda = 0.4980(1)$ Å (all other samples).

TABLE I. Parameters describing the Na$_{1+x}$Al$_x$Ge$_{2-x}$(PO$_4$)$_3$ samples and their thermal history. Glass transition temperature $T_{g,as-prepared}$ and number density $\rho_{as-prepared}$ of the as-prepared glass, crystallization temperature T_x and thermal treatment temperature T_{TT}, time t_{anneal} used to prepare the annealed glass from the as-prepared glass, glass transition temperature $T_{g,annealed}$ and number density $\rho_{annealed}$ of the annealed glass, thermal treatment time t_{cryst} used to crystallize the as-prepared glass, number density $\rho_{crystal}$ of the crystalline phase, and melting point temperature T_{melt}.

x	$T_{g,as-prepared}$ (K)	$\rho_{as-prepared}$ (Å^{-3})	T_x (K)	T_{TT} (K)	t_{anneal} (h)	$T_{g,annealed}$ (K)	$\rho_{annealed}$ (Å^{-3})	t_{cryst} (h)	$\rho_{crystal}$ (Å^{-3})	T_{melt} (K)
0	881(2)	0.0780(1)	926(2)	873(1)	0.25	886(2)	0.0791(1)	17	0.0882(1)	>1523
				876(1)	0.25	$\cdots$	0.0790(1)			
				876(1)	0.5	$\cdots$	0.0798(1)			
0.4	845(2)	0.0774(1)	905(2)	845(1)	2	851(2)	0.0786(1)	17	0.0879(1)	1458(3)
0.8	813(2)	0.0771(1)	896(2)	810(1)	20	810(2)	0.0783(1)	55	0.0885(1)	1362(3)

This instrument was chosen because of its stability and high count-rate over a wide k-range, which enables it to probe small differences in structure.[28] The powdered samples were held in a cylindrical vanadium container of inner diameter 6.8 mm and wall thickness 0.1 mm. Diffraction patterns were measured at room temperature ($\simeq$298 K) for each of the samples in its container, the empty container, the empty instrument, and a cylindrical vanadium rod of diameter 6.08 mm for normalization purposes. The diffraction pattern was also measured for a slab of neutron absorbing $^{10}B_4C$ of dimensions similar to the sample in order to estimate the effect of the sample's attenuation on the background count-rate at small scattering angles.[29] The data analysis followed the procedure described in Ref. 30.

The second set of experiments used the diffractometer GEM at the ISIS pulsed neutron source.[31] This instrument was chosen because it accesses a much larger k_{max} value than D4c, thus improving the resolution of the peaks in $D'(r)$. The powdered samples were held in a cylindrical vanadium container of inner diameter 6 mm and wall thickness 40 μm. Diffraction patterns were measured at room temperature ($\simeq$298 K) for each of the samples in its container, the empty container, the empty instrument, and a cylindrical rod of the alloy $V_{0.9486}Nb_{0.0514}$ (diameter 7.95 mm) for normalization purposes. The datasets were processed using the Gudrun analysis program[32] with inelasticity corrections calculated according to Ref. 33.

In each set of experiments, the relative counting times for the sample-in-container and empty container measurements were optimized in order to minimize the statistical error on the container-corrected intensity.[34] Self-consistency checks were also made to assess the reliability of the measured functions. For instance, it is necessary that (i) each of the measured total structure factors satisfies the sum-rule relation $\int_0^\infty dk\, k^2[S(k) - 1] = -2\pi^2\rho$; (ii) the measured $D'(r)$ functions oscillate about the density line $D'(r) = -4\pi\rho r$ at r-values smaller than the distance of the closest approach between two atoms; and (iii) when these oscillations in $D'(r)$ are set to the density-line values, the back Fourier transform is in good overall agreement with the original total structure factor.

The XRD experiment was performed on beamline 6-ID-D at the Advanced Photon Source with an incident photon energy of 80.019 keV. The scattered x-rays were counted using a Varex 4343CT amorphous silicon flat panel detector, which was placed at a distance of 271.932 mm from the sample position as deduced from the diffraction pattern measured for crystalline CeO_2. The powdered glass samples were held in cylindrical Kapton polyimide tubes of 1.00(1) mm internal diameter and 0.051(6) mm wall thickness. Diffraction patterns were collected for each sample in its container, an empty container, and the empty instrument. The data were converted to one-dimensional diffraction patterns using FIT2D,[35] and the corrections for background scattering, beam polarization, attenuation, and Compton scattering were made using PDFgetX2.[36]

D. Solid-state NMR experiments

Single-pulse ^{27}Al MAS NMR spectra were measured using a Bruker AVANCE 600 spectrometer with a 2.5 mm probe operated at 20.0 kHz. A pulse length of 0.34 μs, corresponding to a flip angle of $\pi/6$ and relaxation delays in the range 0.1–2 s, was used. Chemical shifts are reported against a 1M solution of $Al(NO_3)_3$ using $Al(PO_3)_3$ (isotropic chemical shift δ_{iso} = −20.8 ppm) as a secondary reference. Line shapes were fitted to the Czjzek model[37] simulating a wide distribution of quadrupolar coupling constants, as implemented in DMFit.[38]

Solid-state ^{31}P NMR experiments were performed using an Agilent DD2 spectrometer interfaced with a 5.64 T magnet and a commercial 3.2 mm probe operated at a spinning speed of 10.0 kHz. Chemical shifts are referenced using powdered BPO_4 (δ_{iso} = −29.27 ppm against H_3PO_4 85%) as a secondary reference. Experimental spectra were simulated using the DMFit software.[38] $^{23}Na\{^{31}P\}$ rotational echo double resonance (REDOR) experiments[39] were performed using a Bruker AVANCE 600 spectrometer with a 2.5 mm triple resonance probe and spinning frequency of 10 kHz, operated with the following conditions: ^{23}Na detection using a rotor synchronized Hahn spin-echo sequence with 180° refocusing pulses of 3.25 μs length and a ^{31}P dipolar re-coupling π-pulse of 3.5 μs length, at a spinning speed of 15.0 kHz and a relaxation delay of 1 s. $^{31}P\{^{23}Na\}$ rotational echo adiabatic passage double resonance (REAPDOR) spectra were measured with the same apparatus used for the REDOR experiments and the pulse sequence proposed by Gullion,[40] applying all the 180° pulses on the ^{31}P detection channel and the adiabatic passage pulse (1/3 of the length of the rotor period) to the ^{23}Na nuclei. Spinning and nutation frequencies were 10.0 and 80 kHz, respectively.
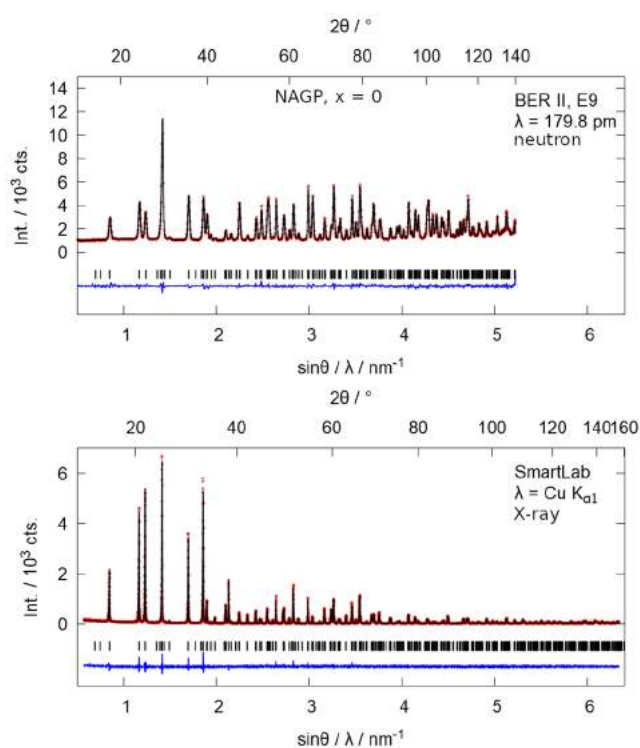
IV. RESULTS

A. Powder diffraction

The NASICON aristotype crystallizes into space group-type $R\bar{3}c$, as originally determined by Hagman and Kierkegaard[41] for $NaZr_2(PO_4)_3$. In the solid solution series $Na_{1+x}Ti_xGe_{2-x}(PO_4)_3$ at room temperature, the boundary phases $NaTi_2(PO_4)_3$ (NTP) and $NaGe_2(PO_4)_3$ (NGP) crystallize into this structure-type and the lower symmetry form $R\bar{3}$, respectively.[2,42] The $R\bar{3}c$ and $R\bar{3}$ space groups have a group–subgroup relation that leads to a splitting of crystallographic sites. According to the literature, the solid solutions crystallize into the NGP-type phase for $x \leq 1$ or the NTP-type phase for $x > 1$.[2,42,43]

The crystal structures of the NAGP compounds were refined using the Rietveld method. The x = 0 and x = 0.4 compositions were assigned to the NGP-type structure, whereas the x = 0.8 composition was assigned to the higher symmetry NTP-type structure. The Rietveld refinements are shown in Figs. 1–3 where, for each experiment, the intensity is plotted vs $\sin\theta/\lambda = k/4\pi$ and 2θ is the scattering angle.[15] The corresponding crystal structure data are summarized in Tables II–IV where SOF represents a site occupation factor; B_{iso} represents a Debye–Waller factor; and R_{exp}, R_p, and R_{wp} represent the expected, profile, and weighted profile R-factors,[44] respectively.

The crystalline NAGP compounds were found to be almost phase pure. For the x = 0 sample, the XRD pattern shows some peaks from a non-determined impurity phase, but according to the peak intensities, the phase fraction is <1%. For the x = 0.4 sample, no impurities could be identified. For the x = 0.8 sample, some impurity peaks and shoulders are present and the intensities suggest a phase fraction of a few percent. The diffraction background for the

FIG. 1. Rietveld refinement results for the crystal structure of NAGP with $x = 0$. Each panel shows the measured intensity I_{obs} (red curve), calculated intensity I_{calc} (black curve), and difference of intensities $I_{obs} - I_{calc}$ (blue curve), along with the positions of the Bragg reflections allowed by the space group for the structure (vertical black bars). The refined composition is $Na_{0.99(2)}Ge_{1.96(2)}(PO_4)_3$, and the refinement details are given in Table II.
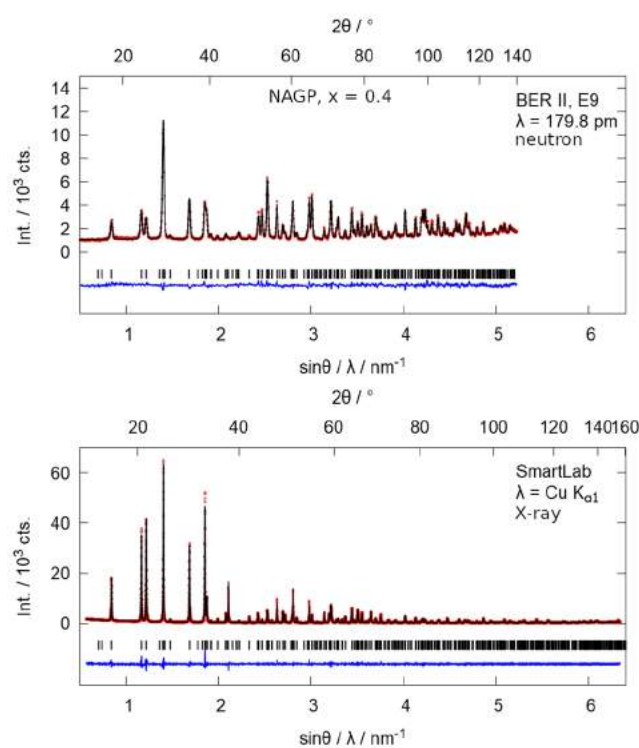
FIG. 2. Rietveld refinement results for the crystal structure of NAGP with $x = 0.4$. Each panel shows the measured intensity I_{obs} (red curve), calculated intensity I_{calc} (black curve), and difference of intensities $I_{obs} - I_{calc}$ (blue curve), along with the positions of the Bragg reflections allowed by the space group for the structure (vertical black bars). The refined composition is $Na_{1.42(2)}Al_{0.43}Ge_{1.57(2)}(PO_4)_3$, and the refinement details are given in Table III.

$x = 0$ and $x = 0.4$ samples is flat, which suggests full crystallization. The background for the $x = 0.8$ sample is increased slightly, suggesting some amorphous residue.

Maldonado-Manso et al.[43] reported differences between the nominal and actual compositions of NAGP and related compounds prepared via a solid-state reaction. To check for non-stoichiometry, different refinement strategies were tested. In the initial model, only the phosphorus SOF was set to unity. Refinement did not show any indication for non-stoichiometry at the oxygen sites, so the occupancies of these sites were also set to unity. The germanium site occupancies for the $x = 0$ sample were refined and showed negligible deviation from full occupancy. Hence, for the aluminum substituted samples, the combined occupation factor SOF(Ge) + SOF(Al) for each site was set to unity, but the Al/Ge-ratio was allowed to vary. The diffraction patterns for the $x = 0$ sample can be reproduced with two fully occupied sodium sites Na(1) and Na(2). Nevertheless, the aluminum substituted samples show occupancy of an additional Na(3) site. Accordingly, this site was included in the refinement of the $x = 0$ data with coordinates fixed at those obtained for the $x = 0.4$ sample. The refinement showed the Na(3) site to be unoccupied within the estimated standard deviation. For the NAGP samples with nominal compositions $x = 0$, 0.4, and 0.8,

the refined compositions were found to be $Na_{0.99(2)}Ge_{1.96(2)}(PO_4)_3$, $Na_{1.42(2)}Al_{0.43}Ge_{1.57(2)}(PO_4)_3$, and $Na_{1.72(2)}Al_{0.804}Ge_{1.196(12)}(PO_4)_3$, respectively.

The crystal structures obtained from powder diffraction are illustrated in Fig. 4. They serve as a starting point for interpreting the pair-distribution functions. A summary of the coordination numbers and bond lengths is given in Table V.

The structures have a single phosphorus site in which a phosphorus atom is coordinated tetrahedrally by four symmetry independent oxygen atoms. The tetrahedra are quite regular with a narrow distribution of P–O distances ranging from 1.50 to 1.54 Å. The phosphorus site occupation was set to unity in all the Rietveld refinements.

In the lower symmetry $R\bar{3}$ structure, there are two sixfold coordinated germanium sites. The Ge(1) site has three O(1) and three O(3) neighbors, while the Ge(2) site has three O(2) and three O(4) neighbors. In the higher symmetry $R\bar{3}c$ structure, the germanium sites are equivalent, i.e., Ge(1) = Ge(2) and O(1) = O(2) with O(3) = O(4). The octahedra are fairly regular with a narrow distribution of Ge–O distances ranging from 1.83 to 1.90 Å for all compounds. Sixfold coordinated Ge^{4+} and Al^{3+} ions have similar ionic radii of 0.67 and 0.675 Å,[45] respectively, so no change in
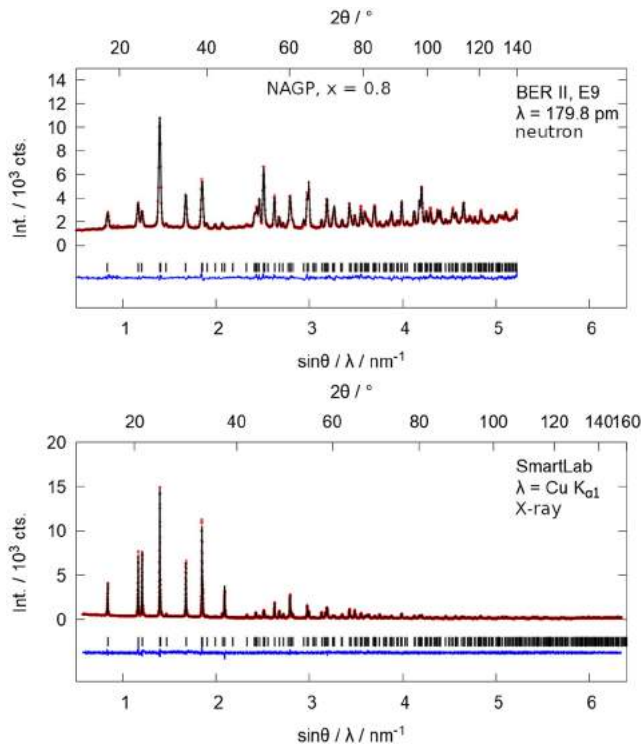
FIG. 3. Rietveld refinement results for the crystal structure of NAGP with $x = 0.8$. Each panel shows the measured intensity I_{obs} (red curve), calculated intensity I_{calc} (black curve), and difference of intensities $I_{obs} - I_{calc}$ (blue curve), along with the positions of the Bragg reflections allowed by the space group for the structure (vertical black bars). The refined composition is $Na_{1.72(2)}Al_{0.804}Ge_{1.196(12)}(PO_4)_3$, and the refinement details are given in Table IV.

bond lengths is expected as Ge is substituted by Al in the NAGP compounds.

In the lower symmetry $R\bar{3}$ structure, there are two sixfold coordinated sodium sites Na(1) and Na(2). The Na(1) site is at the center

of a trigonal prism formed by six symmetry equivalent oxygen atoms O(3), and the Na(2) site is similarly coordinated by O(4) oxygen atoms. In the higher symmetry $R\bar{3}c$ structure, the Na(1) and Na(2) sites are equivalent. In the $x = 0$ and $x = 0.4$ compounds, the Na(1) site is fully occupied and the SOF was set to unity during the last refinement cycle. The Na(2) site is almost fully occupied and was refined. In the $x = 0.8$ compound, the single Na(1)/Na(2) site is fully occupied and its SOF was set to unity. The Na(1)–O and Na(2)–O distances are similar in all three compounds, ranging from 2.39 to 2.52 Å. The crystal structures also have a low-symmetry Na(3) site at the center of an irregular polyhedron of eight oxygen atoms with a broad distribution of Na(3)–O distances ranging from 2.04 to 2.78 Å (Table V). This Na(3) site also has two phosphorus atoms at a similar distance (2.6–2.8 Å) to several of the oxygen atoms, and there is a third Na(3)–P distance of about 3 Å, which is slightly shorter than the Na–Na and the Na–Ge/Al distances. In the $x = 0$ compound, the Na(3) sites are unoccupied. In the $x = 0.4$ and $x = 0.8$ compounds, however, the Na(3) site occupancy is 14% vs 24%, respectively. According to the review by Guin and Tietz,[7] the sodium ions move from Na(1) to Na(2) sites via Na(3) sites. The high mobility leads to large Debye–Waller factors for the sodium atoms.

B. NMR spectroscopy

The ^{31}P MAS NMR spectra taken for both the glassy and crystallized NAGP samples with $x = 0$, 0.4, and 0.8 confirm the results obtained in previous work.[12] The datasets for the $x = 0$ composition are shown in Fig. 5. The spectrum for the as-prepared glass is about 25 ppm wide and somewhat asymmetric. Its center of gravity [−28.9 ppm, Fig. 5(a)] suggests that $P^{(3)}$ units are the majority phosphate species,[12] where the superscript denotes the number of BO atoms per P atom. The spectrum differs significantly from that measured for the crystalline state [−37.4 ppm, Fig. 5(d)], indicating that the local structures in the glassy and crystalline materials are quite different. For the crystal, the chemical shift of −37.4 ppm characterizes a $P_{4Ge}^{(4)}$ unit, in which phosphorus is connected to four sixfold coordinated Ge atoms. The spectrum of the as-prepared glass can be deconvoluted into two Gaussian components at −25.3 and

TABLE II. Crystal structure of $Na_{0.99(2)}Ge_{1.96(2)}(PO_4)_3$ (NAGP with $x = 0$) obtained from the simultaneous refinement of x-ray and neutron diffraction data. Space group $R\bar{3}$, $a = b = 8.10363(18)$ Å, $c = 21.5362(7)$ Å, $\alpha = \beta = 90°$, $\gamma = 120°$, $R_{exp} = 2.35$, $R_p = 2.82$, and $R_{wp} = 3.52$.

Atom	Wyckoff-site	x	y	z	SOF	B_{iso} (Å^2)
Na(1)	3a	0	0	0	1	1.25(19)
Na(2)	3b	0	0	1/2	0.965(19)	4.0(4)
Na(3)	18f	0.0367	1/3	0.0802	0.004(5)	4.0
Ge(1)	6c	0	0	0.14380(11)	0.973(7)	0.68(7)
Ge(2)	6c	0	0	0.35227(10)	0.982(7)	0.62(6)
P(1)	18f	0.2856(3)	0.0012(5)	0.25105(19)	1	0.80(4)
O(1)	18f	0.0150(5)	0.1976(5)	0.18974(17)	1	1.174(8)
O(2)	18f	0.2166(5)	0.0733(5)	0.30457(15)	1	1.17(7)
O(3)	18f	0.1703(5)	0.1875(5)	0.08814(15)	1	0.98(7)
O(4)	18f	0.1348(5)	0.2076(5)	0.40533(14)	1	0.82(7)

TABLE III. Crystal structure of $Na_{1.42(2)}Al_{0.43}Ge_{1.57(2)}(PO_4)_3$ (NAGP with $x = 0.4$) obtained from the simultaneous refinement of x-ray and neutron diffraction data. Space group $R\bar{3}$, $a = b = 8.2218(4)$ Å, $c = 21.4570(15)$ Å, $\alpha = \beta = 90°$, $\gamma = 120°$, $R_{exp} = 2.39$, $R_p = 3.65$, and $R_{wp} = 4.59$.

Atom	Wyckoff-site	x	y	z	SOF	B_{iso} (Å^2)
Na(1)	3a	0	0	0	1	1.41(19)
Na(2)	3b	0	0	1/2	0.964(14)	6.8(5)
Na(3)	18f	0.037(2)	1/3	0.080(5)	0.144(7)	8.5(10)
Ge(1)	6c	0	0	0.145 60(17)	0.800(10)	0.59(9)
Al(1)	6c	0	0	$= x$(Ge1)	$= [1 - $SOF(Ge1)$]$	$= B_{iso}$(Ge1)
Ge(2)	6c	0	0	0.353 60(18)	0.768(9)	1.29(9)
Al(2)	6c	0	0	$= x$(Ge2)	$= [1 - $SOF(Ge2)$]$	$= B_{iso}$(Ge2)
P(1)	18f	0.0046(6)	0.2877(3)	0.250 0(3)	1	1.16(7)
O(1)	18f	0.0272(8)	0.1999(10)	0.191 6(3)	1	2.17(17)
O(2)	18f	0.2134(9)	0.0585(8)	0.306 7(3)	1	1.57(15)
O(3)	18f	0.1827(7)	0.1727(7)	0.088 8(2)	1	1.04(13)
O(4)	18f	0.1457(8)	0.1977(8)	0.406 5(3)	1	1.79(14)

−36.5 ppm having an area ratio of roughly 2:1 (Table VI), consistent with the prediction of the structural model to be introduced in Sec. V C.

There are, however, many other possibilities for deconvoluting the ^{31}P MAS NMR spectrum into two Gaussians. Independent evidence in favor of this particular deconvolution is therefore required. Such evidence is provided by a REAPDOR experiment[40] where, in the ^{31}P{^{23}Na} double resonance experiment conducted here, the magnetic dipole–dipole coupling strength between the observed ^{31}P nuclei and the surrounding ^{23}Na nuclei was probed. This magnetic dipole coupling, which is averaged out by magic-angle spinning, can be re-introduced by irradiating the ^{23}Na nuclei on resonance during the rotor period, resulting in a decrease in signal intensity. A comparison is then made between the intensities S_0 of the regular MAS NMR signal and S of the MAS NMR signal observed with simultaneous irradiation of the ^{23}Na nuclei for a fixed dipolar re-coupling time. The corresponding difference in signal intensity $\Delta S = S_0 - S$ depends on the strength of the dipolar coupling between the ^{31}P and ^{23}Na sites and thus has the potential to distinguish between different local environments in a glass.

Figure 6 shows the Fourier transforms of the echoes obtained after a 1.4 ms mixing time in NAGP glass with $x = 0$. The data indicate that the dipolar dephasing is indeed non-uniform as a function of the isotropic chemical shift: The ^{31}P nuclei on the high-frequency side of the resonance display stronger dipolar dephasing than those on the low-frequency side. Based on these data, it was possible to achieve a consistent deconvolution of the echo signal with dipolar dephasing (which emphasizes the less-strongly coupled ^{31}P nuclei) and the difference signal ΔS (which emphasizes the more-strongly coupled ^{31}P nuclei), in terms of two line shape components near −27(2) and −37(1) ppm (see Fig. 6). Table VI summarizes the line shape parameters for the two-component fit for the single-pulse spectra and the REAPDOR data. In the latter experiments, the ratio of areas of the high-frequency component to the low-frequency component was found to be lower than 2:1 for the S signal and higher than 2:1 for the ΔS signal, consistent with the difference in dipolar coupling strengths between the two sites. The component near −27 ppm is identified with P$^{(3)}$ units, and the component near −37 ppm is identified with P$^{(4)}$ units. The chemical shift of the latter is close to that found for the P$^{(4)}$ units in the crystalline state.

TABLE IV. Crystal structure of $Na_{1.72(2)}Al_{0.804}Ge_{1.196(12)}(PO_4)_3$ (NAGP with $x = 0.8$) obtained from the simultaneous refinement of x-ray and neutron diffraction data. Space group $R\bar{3}c$, $a = b = 8.2927(3)$ Å, $c = 21.4139(12)$ Å, $\alpha = \beta = 90°$, $\gamma = 120°$, $R_{exp} = 2.16$, $R_p = 2.71$, and $R_{wp} = 3.45$. Atomic labels are given according to the crystal structures for $x = 0$ and $x = 0.4$, which are of lower symmetry.

Atom	Wickoff-site	x	y	z	SOF	B_{iso} (Å^2)
Na(1)/Na(2)	6b	0	0	0	1	5.51(16)
Na(3)	18e	0.6455(14)	0	1/4	0.241(6)	3.8(5)
Ge(1)/Ge(2)	12c	0	0	0.146 14(6)	0.598(5)	0.87(7)
Al(1)/Al(2)	12c	0	0	$= z$(Ge1/2)	0.402(5)	$= B_{iso}$(Ge1/2)
P(1)	18e	0.2854(2)	0	1/4	1.000	1.12(6)
O(1)/O(2)	36f	0.0400(3)	0.2043(3)	0.191 42(10)	1.000	1.71(6)
O(3)/O(4)	36f	0.1896(3)	0.1599(3)	0.091 06(10)	1.000	1.61(6)
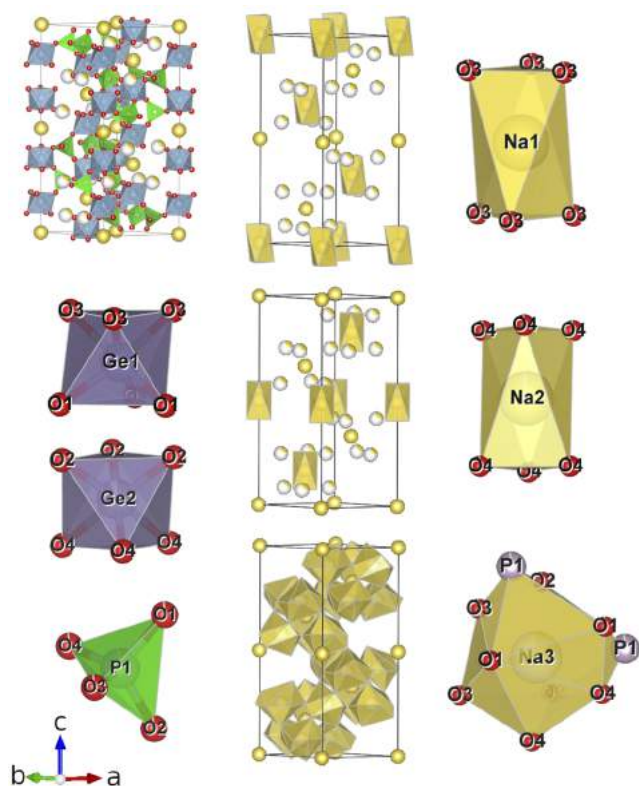
FIG. 4. The R$\bar{3}$-type NAGP crystal structure. The unit cell is shown top left, the GeO$_6$-octahedra are shown middle left, and the PO$_4$-tetrahedron is shown bottom left. The different sodium centered polyhedra are shown on the right. The positions of the different sodium centered polyhedra in the unit cell are shown in the center. In the higher symmetry R$\bar{3}$c structure, several of the sites are equivalent: Ge(1) = Ge(2), Na(1) = Na(2), O(1) = O(2), and O(3) = O(4).
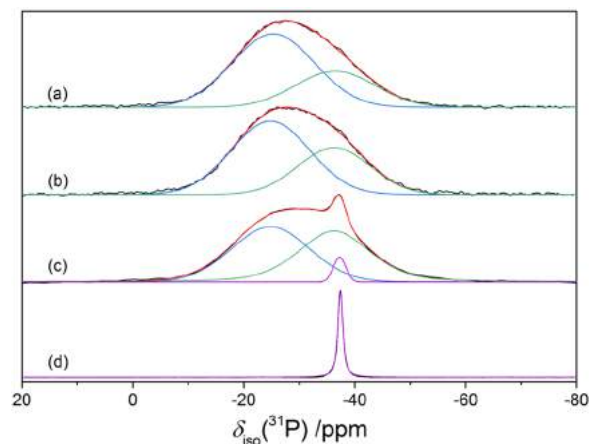
FIG. 5. The single-pulse ^{31}P MAS NMR spectra (black curves) measured for the NAGP materials with $x = 0$: (a) as-prepared glass, (b) glass annealed at $T_{TT} = 873$ K for 0.25 h, (c) glass annealed at $T_{TT} = 876$ K for 0.5 h, and (d) crystalline material. In (a)–(c), the spectra are fitted to two Gaussian peaks (blue and green curves) with the ratio of areas listed in Table VI. In (c), an additional small peak (violet curve) is included to account for a small amount of crystalline material. The sum of fitted functions is given by the red curve. In (d), the spectrum is fitted to a Gauss–Lorentz curve.

Figures 5(b) and 5(c) show the ^{31}P MAS NMR spectra for the annealed glasses with composition $x = 0$. In the case of the sample annealed at 873 K for 0.25 h, the data clearly show that the material remains completely amorphous. Some subtle line shape changes are, however, evident (Fig. S1), which may be attributed to a structural re-arrangement in the glass caused by the onset of the nucleation process. For example, the full-width at half-maximum (FWHM) of the line shape increases from 21.7(5) ppm for the as-prepared glass

TABLE V. Element–oxygen distances for the first coordination spheres in crystalline NAGP with $x = 0$, 0.4, or 0.8.

Atom pair	Multiplicity	$x = 0$ Distance (Å)	$x = 0.4$ Distance (Å)	$x = 0.8$ Distance (Å)
Na(1)–O(3)	6×	2.392(4)	2.402(4)	2.439(2)
Na(2)–O(4)	6×	2.518(3)	2.481(6)	2.439(2)
Na(3)–O(1)			2.62(10)	2.582(11)
–O(1)			2.78(5)	2.588(5)
–O(2)			2.50(5)	2.582(11)
–O(2)			2.53(10)	2.588(5)
–O(3)			2.191(18)	2.200(3)
–O(3)			2.344(10)	2.463(13)
–O(4)			2.038(10)	2.200(3)
–O(4)			2.487(16)	2.463(13)
Ge(1)/Al(1)–O(1)	3×	1.827(5)	1.833(8)	1.832(3)
–O(3)	3×	1.882(4)	1.904(5)	1.881(2)
Ge(2)/Al(2)–O(2)	3×	1.855(5)	1.865(7)	1.832(3)
–O(4)	3×	1.863(4)	1.849(8)	1.881(2)
P–O(1)		1.534(6)	1.503(9)	1.537(3)
–O(2)		1.520(6)	1.541(8)	1.537(3)
–O(3)		1.520(4)	1.531(8)	1.528(2)
–O(4)		1.543(6)	1.514(6)	1.528(2)

TABLE VI. Deconvolution of the ^{31}P MAS-NMR spectra for glassy (as-prepared vs annealed) and crystalline NAGP with $x = 0$. The parameters describe the fractional area, δ_{iso}, and FWHM of the peaks fitted to the spectra. For one of the annealed glasses, the crystalline contribution to the line shape is indicated by a subscript. The errors on the fitted areas are ±1% for the single-pulse spectra vs ±5% for the REAPDOR line shapes. The errors on δ_{iso} and the FWHM are ±0.5 ppm for the single-pulse spectra vs ±2 ppm for the REAPDOR line shapes.

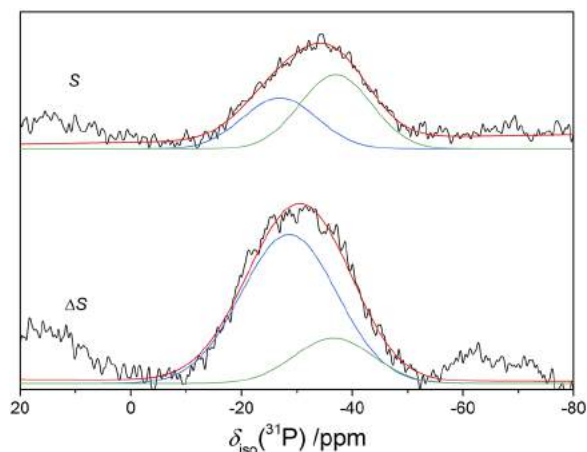| Material	Fitted spectrum	Species	Area (%)	δ_{iso} (ppm)	FWHM (ppm)
Glass: As-prepared	Single-pulse	$P^{(3)}$	68	−25.3	17.5
		$P^{(4)}$	32	−36.5	16.9
Glass: As-prepared	REAPDOR S	$P^{(3)}$	42	−26.9	15.8
		$P^{(4)}$	58	−37.0	15.3
Glass: As-prepared	REAPDOR ΔS	$P^{(3)}$	80	−28.6	20.3
		$P^{(4)}$	20	−36.6	17.0
Glass: Annealed at T_{TT} = 873 K for 0.25 h	Single-pulse	$P^{(3)}$	63	−24.8	16.6
		$P^{(4)}$	37	−36.3	15.3
Glass: Annealed at T_{TT} = 876 K for 0.25 h	Single-pulse	$P^{(3)}$	61	−24.8	17.0
		$P^{(4)}$	39	−36.3	15.5
Glass: Annealed at T_{TT} = 876 K for 0.5 h	Single-pulse	$P^{(3)}$	49	−24.8	17.0
		$P^{(4)}$	48	−36.3	15.3
		$P^{(4)}_{cryst}$	3	−37.3	2.7
Crystal	Single-pulse	$P^{(4)}$	100	−37.4	1.0

to 22.8(5) ppm for the annealed glass. Table VI indicates that the change to the principal line shape involves a change to the ratio of the relative areas of the two line shape components, indicating a moderate increase in the fraction of $P^{(4)}$ units having the same local coordination environment as the crystalline phase. This finding was confirmed by fixing the chemical shifts and linewidths for the $P^{(3)}$ and $P^{(4)}$ sites at the average of the values listed in Table VI for

FIG. 6. The ^{31}P{^{23}Na} REAPDOR results for NAGP glass with $x = 0$. The Fourier transforms of S (top) and $\Delta S = S_0 - S$ (bottom) are plotted, where the spectra were obtained for a dipolar mixing time of 1.4 ms. Each spectrum is fitted to two Gaussian peaks (blue and green curves), and the sum of fitted functions is given by the red curve. The weaker signals are attributed to spinning sidebands.

the as-prepared and annealed glasses and fitting the spectra for both glassy samples with the peak areas as the only adjustable parameters. The peak areas showed a change in the ratio of $P^{(4)}$:$P^{(3)}$ sites from 33.5(1.0):66.5(1.0) for the as-prepared glass to 36.0(1.0):64.0(1.0) for the annealed glass. In the case of the sample annealed at 876 K for 0.5 h, the change in peak areas is more dramatic, with the $P^{(4)}$:$P^{(3)}$ ratio increasing to ~1:1. For this sample, a small amount of crystalline material is also detected.
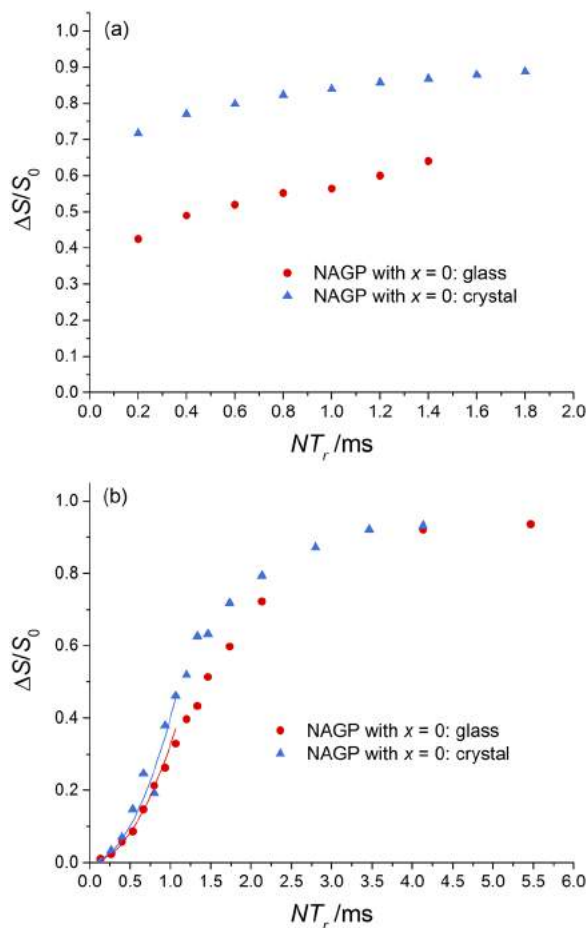
Finally, the ^{23}Na/^{31}P double resonance experiments also allow for a comparison between the ^{31}P/^{23}Na dipolar coupling strengths of glassy and crystalline materials by plotting the normalized difference signal as a function of the dipolar mixing time NT_r (= number of rotor cycles × rotor period). The corresponding ^{31}P{^{23}Na} REAPDOR curves are compared in Fig. 7(a) and qualitatively illustrate that the internuclear ^{31}P/^{23}Na dipole–dipole interactions are significantly stronger in the crystalline rather than in the glassy material. A more quantitative estimate can be found on the basis of the ^{23}Na{^{31}P} REDOR results[39] shown in Fig. 7(b). In this experiment, the dephasing of the ^{23}Na nuclei in the dipolar field created by the ^{31}P spins is being observed. The simpler spin dynamics arising from the spin-1/2 character of the recoupled ^{31}P nuclei permits an approximate analysis in terms of dipolar second moments $M_{2(Na-P)}$, using the formula

$$\frac{\Delta S}{S_0} = \frac{4}{3\pi^2}(NT_r)^2 f M_{2(Na-P)} \qquad (8)$$

in the limit of short mixing times when $\Delta S/S_0 \leq 0.2$–0.3,[46] where f is a calibration factor on the order of unity. The quantity $M_{2(Na-P)}$ can be calculated from the internuclear distances using Van Vleck theory;[47] it is proportional to the sum of the inverse sixth powers of all Na–P internuclear distances present and can thus be computed from
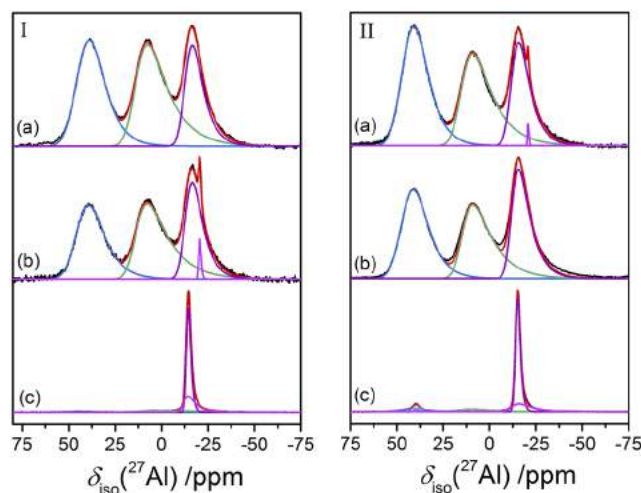
FIG. 7. The (a) ^{31}P{^{23}Na} REAPDOR and (b) ^{23}Na{^{31}P} REDOR datasets for as-prepared glassy vs crystalline NAGP with $x = 0$. In (b), the solid curves show fits to the datasets using Eq. (8) for the data range $\Delta S/S_0 \leq 0.3$. The results indicate consistently that the magnetic dipole–dipole coupling between the nuclei ^{23}Na and ^{31}P is stronger in the crystal as compared to the glass.

FIG. 8. The single-pulse ^{27}Al MAS NMR spectra (black curves) measured for (a) as-prepared glassy, (b) annealed glassy, and (c) crystalline NAGP with (I) $x = 0.4$ or (II) $x = 0.8$. The Czjzek fits to the spectral components are given by the blue or cyan curves for Al(IV), the green curve for Al(V), and the violet or magenta curves for Al(VI). The sum of fitted functions is given by the red curve.

any crystal structure. For crystalline NAGP with $x = 0$, a theoretical value $M_{2(\text{Na–P})} = 4.1 \times 10^6$ rad^2 s^{-2} is expected, and the experimental data obtained by us on this compound indicate an f-value of 0.72. Applying this calibration factor to the REDOR data obtained on the glass gives $M_{2(\text{Na–P})} = 3.3 \times 10^6$ rad^2 s^{-2}, i.e., a 20% lower value as compared to the crystalline compound. It follows that the mean Na–P$^{(4)}$ distance back-calculated from $M_{2(\text{Na–P})}$ in the NAGP crystal is shorter than the average of the Na–P$^{(3)}$ and Na–P$^{(4)}$ distances back-calculated from $M_{2(\text{Na–P})}$ in the glass.

The ^{27}Al MAS NMR spectra taken for the glassy and crystallized NAGP samples with $x = 0.4$ and 0.8 are shown in Fig. 8. The line shapes were fitted using a Czjzek model[37] that accounts for a distribution of quadrupolar coupling constants originating from a distribution of local field gradients. The fitted parameters are listed in Table S1.

For the glasses, the spectra feature broad resonances at isotropic chemical shifts around 46(1), 15(1), and −12(1) ppm that can be attributed to aluminum in fourfold, fivefold, and sixfold coordination environments, respectively. For some of the glassy samples, a sharp peak near −20 ppm is observed, which indicates a small amount of a yet unidentified crystalline impurity with aluminum in sixfold coordination. For the $x = 0.8$ composition, the presence of this site in the as-prepared glass, but its absence in the annealed material, suggests a non-uniform distribution of more ordered regions when the glass is first formed.

For the crystallized materials prepared by thermally annealing the glass for an extended period of time, the ^{27}Al MAS NMR spectra show that crystalline NASICON is the dominant phase. The dataset for the $x = 0.8$ composition shows a small amount of fourfold coordinated aluminum in an AlPO$_4$ impurity phase. The results for both compositions indicate that a small fraction of aluminum atoms remain in a glass-like domain where they occur in all three coordination environments, which contributes toward an average Al–O coordination number less than six (Table VII).

In Table VII, the results for the aluminum speciation are compared to those obtained for a different set of NAGP samples in previous work.[12] For the as-prepared glass, there is some variation in the speciation that may be influenced by the sample preparation procedure although the NMR spectra in Ref. 12 were measured at a lower field strength of 5.7 T (cf. 14.1 T in the present work) where the resolution of the individual ^{27}Al resonances is substantially lower. The results show an increase in the mean Al–O coordination number when the as-prepared glass is thermally annealed.

C. Pair-distribution functions

The $S(k)$ functions measured by ND (using GEM or D4c) and XRD are shown in Figs. 9–12. For the crystalline materials, there are

TABLE VII. The Al speciation in the NAGP materials with $x = 0.4$ and $x = 0.8$ found from the ^{27}Al MAS NMR experiments. The mean Al–O coordination number is also given. The error on the fraction of Al in a fourfold, fivefold, or sixfold coordination environment is $\pm 2\%$ in the present work vs $\pm 3\%$ in Ref. 12. Crystalline coordination environments are identified by a subscript.

x	Material	Al(IV) (%)	Al(IV)$_{cryst}$ (%)	Al(V) (%)	Al(VI) (%)	Al(VI)$_{cryst}$ (%)	$\bar{n}^O_{Al}$	References
0.4	Glass: As-prepared	37.2	$\cdots$	39.8	23.0	$\cdots$	4.86(6)	Present work
		43	$\cdots$	33	20	4	4.81(8)	12
	Glass: Annealed	32.9	$\cdots$	37.9	27.7	1.5	4.96(6)	Present work
	Crystal	2.5	$\cdots$	11.5	25.3	60.8	5.84(8)	
0.8	Glass: As-prepared	39.6	$\cdots$	35.7	24.3	0.4	4.85(6)	Present work
		40	$\cdots$	34	22	4	4.86(8)	12
	Glass: Annealed	36.4	$\cdots$	33.0	30.6	$\cdots$	4.94(6)	Present work
	Crystal	6.8	3.7	6.4	17.6	65.5	5.73(8)	

discrepancies between the intensities of Bragg peaks measured using GEM vs D4c that originate from (i) differences between the k-space resolution function of the diffractometers and (ii) the possibility of some preferred orientation of the crystallites (Fig. 9). For the glassy materials, the GEM and D4c datasets for the as-prepared glasses are in overall agreement (Fig. 10). The XRD patterns indicate a small amount of crystallinity for the annealed

$x = 0$ and $x = 0.8$ samples (Fig. 12) that is not observed using ND with D4c, which may reflect the enhanced k-space resolution of the x-ray diffractometer. For all the glassy materials, the $S(k)$ functions display a shoulder at $k_1 \sim 0.85$ Å^{-1} that is indicative of ordering on a real-space length scale of $2\pi/k_1 \sim 7.4$ Å.
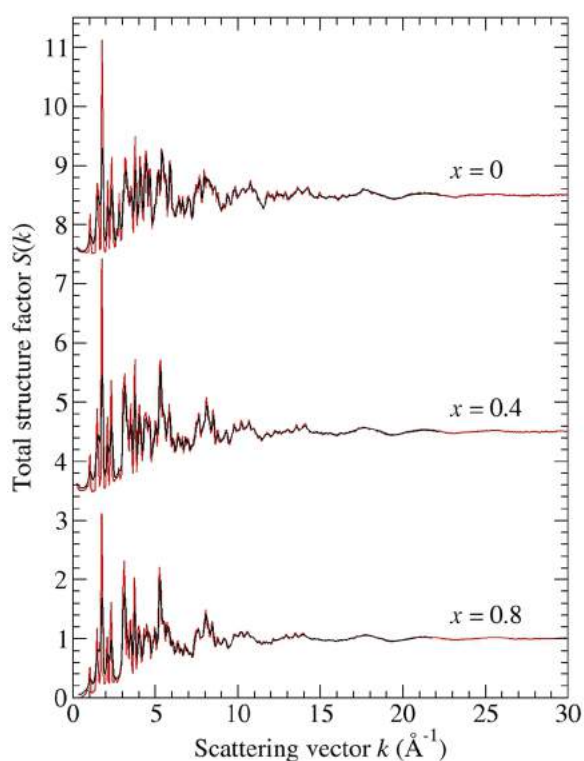
FIG. 9. The total structure factors $S(k)$ for crystalline NAGP with $x = 0$, 0.4, and 0.8 measured using GEM (red curves) or D4c (black curves). The vertical error bars are smaller than the line thickness at most k values. For clarity of presentation, several of the curves are displaced vertically and the GEM datasets are shown only to 30 Å^{-1}.
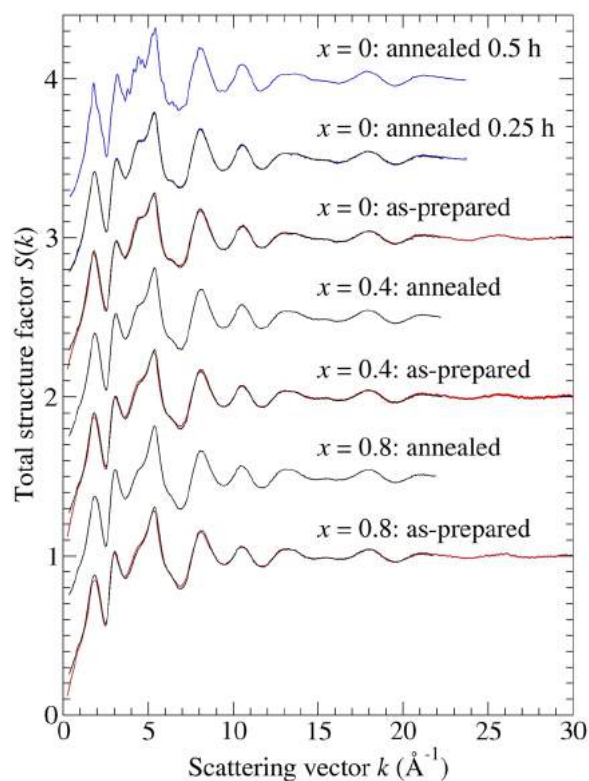
FIG. 10. The total structure factors $S(k)$ for as-prepared vs annealed glassy NAGP with $x = 0$, 0.4, and 0.8. The red curves give the GEM datasets, and the black or blue curves give the D4c datasets, where the latter correspond to the $x = 0$ glass annealed at $T_{TT} = 876$ K for either 0.25 or 0.5 h. The vertical error bars are smaller than the line thickness at most k values. For clarity of presentation, several of the curves are displaced vertically and the GEM datasets are shown only to 30 Å^{-1}.
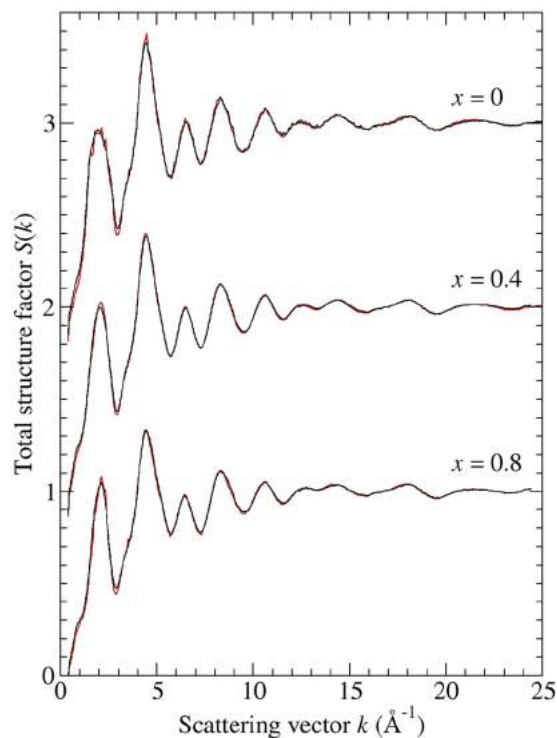
FIG. 11. The total structure factors $S(k)$ for crystalline NAGP with $x = 0$, 0.4, and 0.8 measured using XRD. Several of the curves are displaced vertically for clarity of presentation.
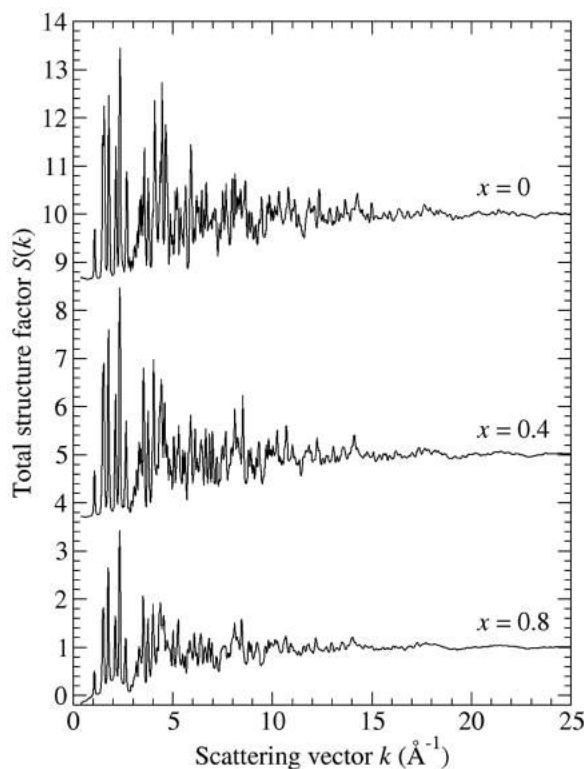
FIG. 12. The total structure factors $S(k)$ for the as-prepared (black curves) vs annealed (red curves) glassy NAGP with $x = 0$, 0.4, and 0.8 measured using XRD. Several of the curves are displaced vertically for clarity of presentation.

In Na$_2$O–GeO$_2$–P$_2$O$_5$ glasses, the appearance of a similar feature has been linked to an inhomogeneous distribution of Na and Ge atoms.[48]

1. Structure of NAGP with x = 0

For crystalline NAGP with $x = 0$, the $D'(r)$ functions measured using GEM and XRD are shown in Fig. 13. By comparison with the powder diffraction work (Table V), the first peak at 1.52 Å and the second peak at 1.86 Å originate from P–O and Ge–O correlations, respectively, and the third peak will have a contribution from both Na–O and O–O correlations. The $D'(r)$ functions were therefore fitted by using the following protocol.

A single peak was used to represent the P–O correlations. A single peak was also used to represent the Ge–O correlations in the ND work, whereas two peaks were used to represent these correlations in the XRD work, where the large atomic number of Ge ($Z = 32$) makes the results particularly sensitive to the germanium coordination environment. A single peak was used to represent the Na–O correlations with a coordination number fixed at the value found from the Rietveld refinement. Two peaks were used to represent the O–O correlations because each BO atom is shared between a PO$_4$ tetrahedron and a GeO$_6$ octahedron, i.e., it has three nearest-neighbor O atoms within a tetrahedron and four nearest-neighbor O atoms at a longer distance within an octahedron (the fifth O atom within an octahedron is at an even longer next nearest-neighbor distance).

The coordination numbers for these peaks were fixed at $\bar{n}_O^O = 3$ and $\bar{n}_O^O = 4$, respectively. The fitted $D'(r)$ functions gave $\bar{n}_P^O = 3.58(5)$ with $\bar{n}_{Ge}^O = 5.98(5)$ for GEM [Fig. 13(b)] vs $\bar{n}_P^O = 3.78(3)$ with $\bar{n}_{Ge}^O = 5.90(1)$ for XRD [Fig. 13(c)]. In comparison, for the $x = 0$ glass, a similar fit to $D'(r)$ using a single Gaussian peak for the P–O correlations gave $\bar{n}_P^O = 3.32(5)$ (GEM) vs $\bar{n}_P^O = 3.61(3)$ (XRD).

The P–O coordination number found from both ND and XRD is smaller than the value $\bar{n}_P^O = 4$ expected from Rietveld refinement and from ^{31}P MAS NMR experiments (Secs. IV A and IV B). In the latter, the measured chemical shifts are typical of phosphorus in a fourfold coordination environment and are quite different to the chemical shift of phosphorus in a PO$_3$ coordination environment, which is observed near 100 ppm in the crystalline molecular systems P$_4$O$_7$ and P$_4$O$_6$S, as referenced to an aqueous solution of H$_3$PO$_4$.[49] A measured P–O coordination number $\bar{n}_P^O < 4$ is typical of diffraction work on phosphate materials,[48,50,51] where the shortfall is often attributed to the k-space resolution of the diffractometer.[19,52]

Several steps were taken in order to investigate the origin of the reduced $\bar{n}_P^O$ values. In this analysis, the GEM dataset for crystalline NAGP with $x = 0$ was used as an exemplar because (i) the large k_{max} value of $\simeq$39 Å^{-1} leads to well-resolved peaks in $D'(r)$, (ii) the analysis is simplified by the absence of Al–O correlations, and (iii) the crystal structure is known.
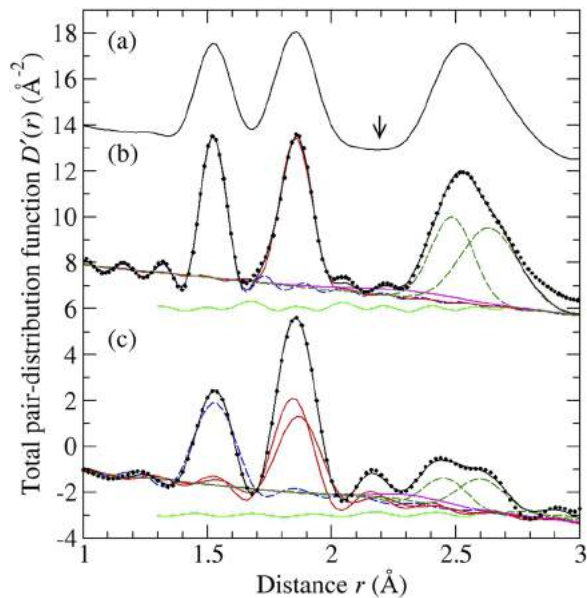
FIG. 13. The $D'(r)$ functions for crystalline NAGP with $x = 0$ as obtained from the GEM data by the application of either (a) a Lorch or (b) a step modification function with $k_{max} = 39.1$ Å^{-1} and from (c) the XRD data by the application of a step modification function with $k_{max} = 24.99$ Å^{-1}. In (a), the vertical downward arrow indicates the minimum after the second peak. In (b) and (c), the measured functions (filled circles) are fitted using a single Gaussian peak to describe the P–O correlations (blue broken curve). The other peaks show the fitted contributions from the Ge–O [red solid curve(s)], Na–O (magenta solid curve), and O–O (green broken curves) correlations. The black solid curves give the overall fits. The displaced green solid curves show the residuals where (b) $R_\chi = 5.06\%$ or (c) $R_\chi = 2.97\%$ for the fitted range 1.30–2.70 Å. In (a) and (b), the curves are displaced vertically for clarity of presentation.

(1) The coherent neutron scattering length of P is reported to be in the range 5.0–5.3 fm[53–55] with a recommended value $b_P = 5.13(1)$ fm.[17] The data analysis was repeated using b_P values that extend over this range, but a notable increase in $\tilde{n}_P^O$ was not observed.

(2) The dataset was reanalyzed using the density $\rho = 0.0843(1)$ Å^{-3} measured by He pycnometry. A fit to the $D'(r)$ function using the strategy reported above led, however, to a reduced coordination number $\tilde{n}_P^O = 3.44(5)$ with $\tilde{n}_{Ge}^O = 5.71(5)$.

(3) The Lorch[20] modification function was used in Eq. (2) to suppress Fourier transform artifacts, which facilitates the extraction of coordination numbers by direct integration over the peaks in $D'(r)$. Here, the mean coordination number of atoms of type β, contained in a volume defined by two concentric spheres of radii r_i and r_j centered on an atom of type α, is given by

$$\tilde{n}_\alpha^\beta = 4\pi \rho c_\beta \int_{r_i}^{r_j} dr\, r^2 g_{\alpha\beta}(r). \tag{9}$$

The resultant $D'(r)$ function is shown in Fig. 13(a). Integration to the first minimum at 1.67 Å gives $\tilde{n}_P^O = 3.7(1)$,

whereas integration to the second minimum at 2.19 Å gives an increased value $\tilde{n}_P^O = 4.3(2)$ if the Ge–O coordination number is set at $\tilde{n}_{Ge}^O = 6$. The measured $D'(r)$ function therefore has sufficient area to accommodate a P–O coordination number of 4, which suggests a broader distribution of P–O distances than found by fitting a single peak.

(4) In view of the findings in step (3), the fitting procedure was adapted to include a second P–O Gaussian peak. This requirement may originate from different coordination environments for the BO atoms in a phosphate tetrahedron. All these BO atoms are shared between P and Ge atoms but only two [O(3) and O(4)] have nearest-neighbor sodium atoms, where the Na–O distance is 2.39–2.52 Å (Table V). The fitted GEM and XRD $D'(r)$ functions are shown in Figs. 14(a) and 15(a), respectively, and the peak parameters are summarized in Tables S2 and S3. Inclusion of the second P–O peak increases the P–O coordination number to $\tilde{n}_P^O \simeq 3.9$ and leads to a Ge–O coordination number $\tilde{n}_{Ge}^O = 5.90(4)$–5.95(5), which compares to an expected value of $\tilde{n}_{Ge}^O = 6$. The Ge–O distance of 1.857(2) Å obtained from ND is in agreement with the mean Rietveld value of 1.857 Å (Table V), and the Ge–O distances of 1.847(1) and 1.871(1) Å obtained from XRD compare to average short and long Rietveld Ge–O distances of 1.841 and 1.873 Å, respectively (Table V).

The GEM results for the crystalline material (Table S2) provided starting parameters for fitting the D4c dataset. The fitted $D'(r)$ function is shown in Fig. 16(a), where the peaks are broadened
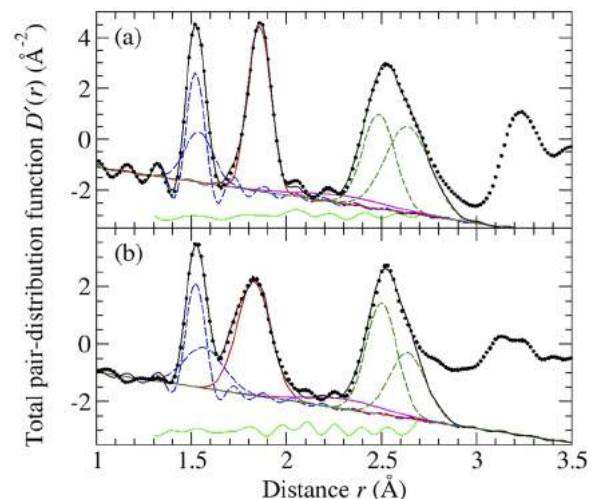
FIG. 14. The fitted $D'(r)$ functions for (a) crystalline and (b) as-prepared glassy NAGP with $x = 0$ measured using GEM. The filled circles give the measured function; the black solid curve gives the fitted function; and the other curves show the contributions from the P–O (blue broken curves), Ge–O (red solid curve), Na–O (magenta solid curve), and O–O (green broken curves) correlations. The displaced green solid curve shows the residual. For the glass, the Na–O and O–O correlations are introduced to constrain the peaks fitted at smaller r-values.
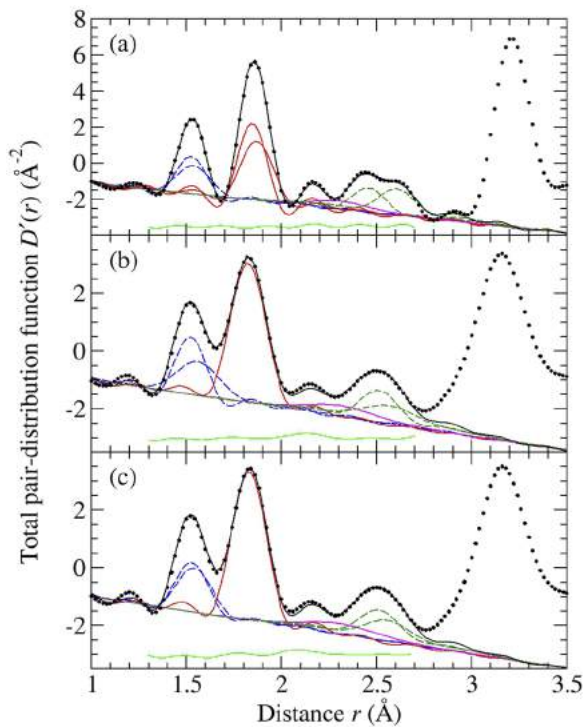
FIG. 15. The fitted $D'(r)$ functions for (a) crystalline, (b) as-prepared glassy, and (c) annealed glassy (T_{TT} = 873 K) NAGP with x = 0 measured using XRD. The filled circles give the measured function; the black solid curve gives the fitted function; and the other curves show the contributions from the P–O (blue broken curves), Ge–O [red solid curve(s)], Na–O (magenta solid curve), and O–O (green broken curves) correlations. The displaced green solid curve shows the residual. For the glass, the Na–O and O–O correlations are introduced to constrain the peaks fitted at smaller r-values.
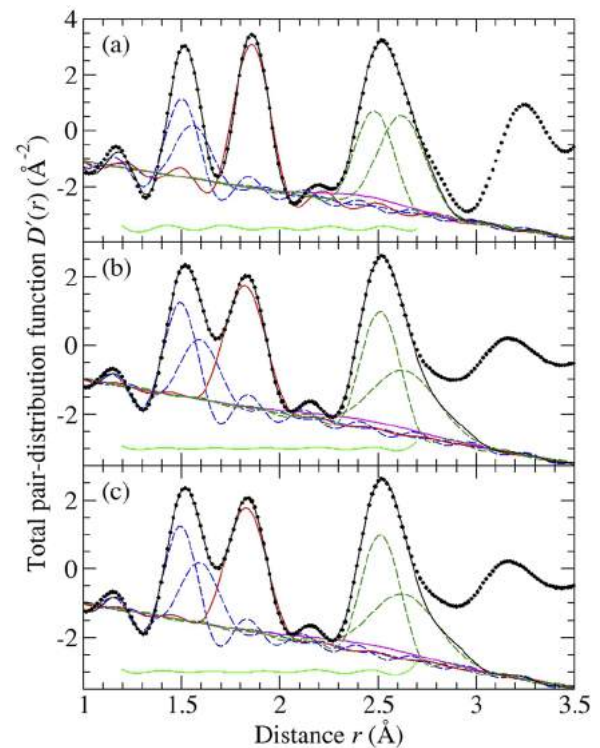
FIG. 16. The fitted $D'(r)$ functions for (a) crystalline, (b) as-prepared glassy, and (c) annealed glassy (T_{TT} = 873 K) NAGP with x = 0 measured using D4c. The filled circles give the measured function; the black solid curve gives the fitted function; and the other curves show the contributions from the P–O (blue broken curves), Ge–O (red solid curve), Na–O (magenta solid curve), and O–O (green broken curves) correlations. The displaced green solid curve shows the residual. For the glass, the Na–O and O–O correlations are introduced to constrain the peaks fitted at smaller r-values.

relative to GEM because of the smaller value k_{max} = 22.25 Å^{-1} of D4c and the peak parameters are summarized in Table S4. The fit gives $\bar{n}_P^O$ = 4.00(4) with $\bar{n}_{Ge}^O$ = 5.97(5).

For the as-prepared glass, the GEM and XRD datasets were fitted using two Gaussian peaks representing the nearest-neighbor P–O correlations and one Gaussian peak representing the nearest-neighbor Ge–O correlations. Additional peaks at larger-r values were used in order to constrain the fitted functions at lower r. The fitted $D'(r)$ functions are shown in Fig. 14(b) (ND) and Fig. 15(b) (XRD), and the P–O and Ge–O peak parameters are summarized in Tables S5 and S6. The GEM results provided starting parameters for fitting the D4c dataset for the as-prepared glass, where the fitted $D'(r)$ function is shown in Fig. 16(b) and the P–O and Ge–O peak parameters are summarized in Table S7. The results give a P–O coordination number of $\bar{n}_P^O$ = 4 within the experimental error and an average Ge–O coordination number $\bar{n}_{Ge}^O$ ~ 5 that is significantly smaller than found for the crystalline phase.

For the annealed glass, the fits were initiated using starting parameters obtained for the as-prepared glass. The fitted $D'(r)$ functions are shown in Fig. 15(c) (XRD) and in Fig. 16(c) and

Fig. S2 (ND). The P–O and Ge–O peak parameters are summarized in Tables S8 and S9. The results do not indicate a change to $\bar{n}_P^O$ but show that, relative to the as-prepared glass, $\bar{n}_{Ge}^O$ increases with the time of thermal annealing.

### 2. Structure of NAGP with x > 0

The GEM and XRD $D'(r)$ functions for crystalline and glassy NAGP with x = 0.4 and x = 0.8 are shown in Figs. 17–20. By comparison with the powder diffraction results (Table V), the first peak in each $D'(r)$ function at ≃1.52 Å is attributed to P–O correlations, the second peak at ≃1.86 Å will have contributions from both Ge–O and Al–O correlations, and the third peak will have contributions from both Na–O and O–O correlations. In view of the results obtained in Sec. IV C 1, the nearest-neighbor P–O correlations in $D'(r)$ were represented by two Gaussian peaks. The parameters describing the Gaussian peaks for the nearest-neighbor Al–O correlations were constrained using the information obtained from other techniques.

For the crystalline materials, the Al–O coordination number was fixed at $\bar{n}_{Al}^O$ = 6 and the position of the Gaussian peak
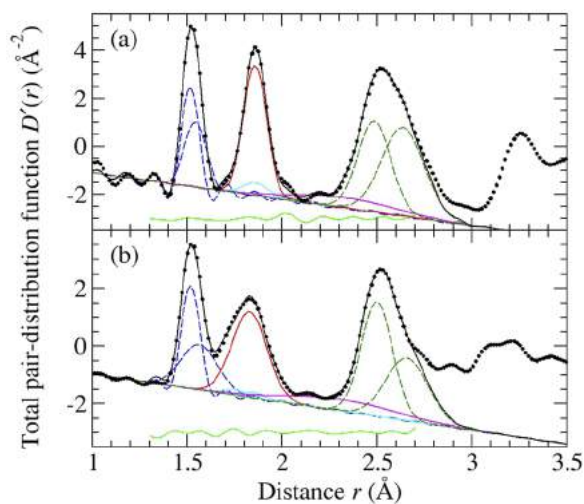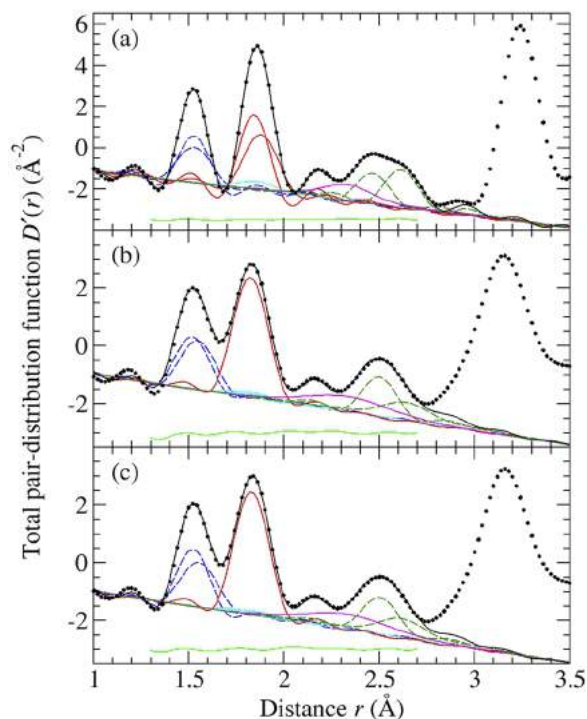
FIG. 17. The fitted $D'(r)$ functions for (a) crystalline and (b) as-prepared glassy NAGP with $x = 0.4$ measured using GEM. The filled circles give the measured function; the black solid curve gives the fitted function; and the other curves show the contributions from the P–O (blue broken curves), Al–O (cyan solid curves), Ge–O (red solid curve), Na–O (magenta solid curve), and O–O (green broken curves) correlations. The displaced green solid curve shows the residual. For the glass, the Na–O and O–O correlations are introduced to constrain the peaks fitted at smaller r-values.

was set at the mean nearest-neighbor Al–O distance of 1.86 Å found from powder diffraction (Table V). The third peak was treated in the same way as $D'(r)$ for crystalline NAGP with $x = 0$. The fitted GEM $D'(r)$ functions for the $x = 0.4$ and $x = 0.8$
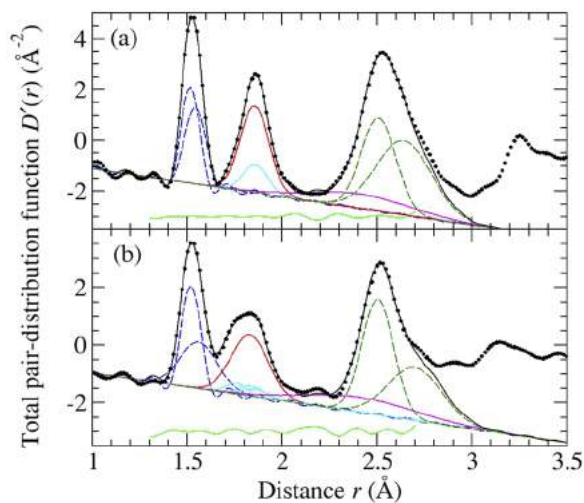
FIG. 18. The fitted $D'(r)$ functions for (a) crystalline and (b) as-prepared glassy NAGP with $x = 0.8$ measured using GEM. The filled circles give the measured function; the black solid curve gives the fitted function; and the other curves show the contributions from the P–O (blue broken curves), Al–O (cyan solid curves), Ge–O (red solid curve), Na–O (magenta solid curve), and O–O (green broken curves) correlations. The displaced green solid curve shows the residual. For the glass, the Na–O and O–O correlations are introduced to constrain the peaks fitted at smaller r-values.
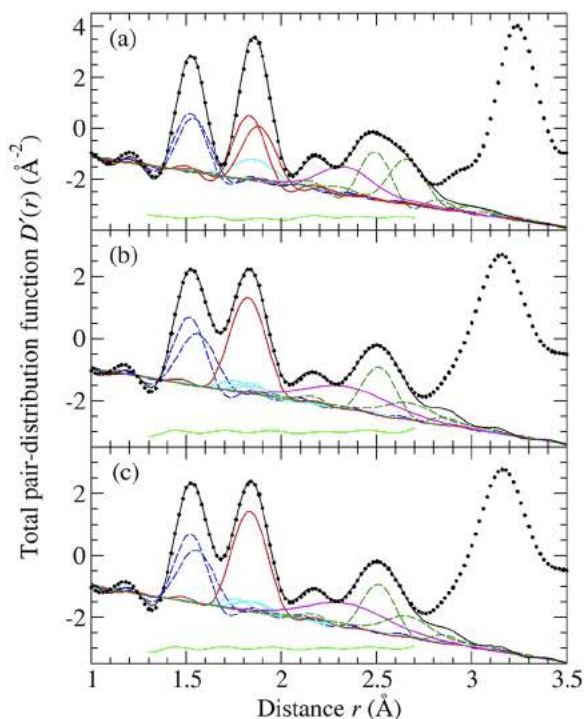

FIG. 19. The fitted $D'(r)$ functions for (a) crystalline, (b) as-prepared glassy, and (c) annealed glassy NAGP with $x = 0.4$ measured using XRD. The filled circles give the measured function; the black solid curve gives the fitted function; and the other curves show the contributions from the P–O (blue broken curves), Al–O (cyan solid curves), Ge–O [red solid curve(s)], Na–O (magenta solid curve), and O–O (green broken curves) correlations. The displaced green solid curve shows the residual. For the glass, the Na–O and O–O correlations are introduced to constrain the peaks fitted at smaller r-values.

compositions are shown in Figs. 17(a) and 18(a), respectively, and the peak parameters are summarized in Table S2. The fitted XRD $D'(r)$ functions for the $x = 0.4$ and $x = 0.8$ compositions are shown in Figs. 19(a) and 20(a), respectively, and the peak parameters are summarized in Table S3. The P–O coordination numbers are in the range 3.85(3)–3.99(3), and within the experimental error, the Ge–O coordination number is consistent with the powder diffraction value $\bar{n}_{Ge}^{O} = 6$.

The GEM results (Table S2) provided starting parameters for fitting the D4c datasets for the crystalline materials. The fitted $D'(r)$ functions for the $x = 0.4$ and $x = 0.8$ compositions are shown in Figs. 21(a) and 22(a), respectively, and the fitted P–O and Ge–O parameters are summarized in Table S4. The fitted coordination numbers are $\bar{n}_{P}^{O} = 4$ and $\bar{n}_{Ge}^{O} = 6$ within the experimental error.

For the glassy materials, three Gaussian peaks were used to represent the nearest-neighbor Al–O correlations for fourfold, fivefold, and sixfold coordinated aluminum atoms. The relative abundance of these species was fixed in accordance with the aluminum speciation found from ^{27}Al MAS NMR experiments (Table VII). The peak positions for fourfold and fivefold coordinated aluminum atoms were set
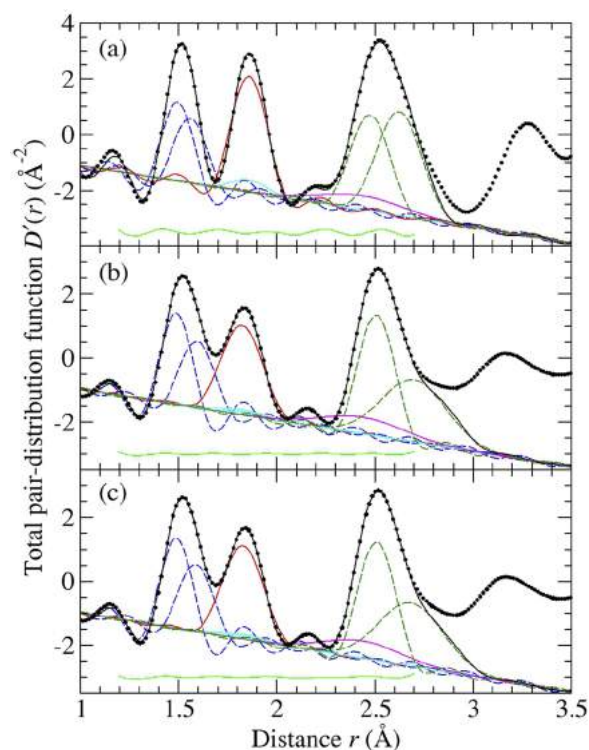
FIG. 20. The fitted $D'(r)$ functions for (a) crystalline, (b) as-prepared glassy, and (c) annealed glassy NAGP with $x = 0.8$ measured using XRD. The filled circles give the measured function; the black solid curve gives the fitted function; and the other curves show the contributions from the P–O (blue broken curves), Al–O (cyan solid curves), Ge–O [red solid curve(s)], Na–O (magenta solid curve), and O–O (green broken curves) correlations. The displaced green solid curve shows the residual. For the glass, the Na–O and O–O correlations are introduced to constrain the peaks fitted at smaller r-values.

FIG. 21. The fitted $D'(r)$ functions for (a) crystalline, (b) as-prepared glassy, and (c) annealed glassy NAGP with $x = 0.4$ measured using D4c. The filled circles give the measured function; the black solid curve gives the fitted function; and the other curves show the contributions from the P–O (blue broken curves), Al–O (cyan solid curves), Ge–O (red solid curve), Na–O (magenta solid curve), and O–O (green broken curves) correlations. The displaced green solid curve shows the residual. For the glass, the Na–O and O–O correlations are introduced to constrain the peaks fitted at smaller r-values.

at 1.76 and 1.84 Å, respectively, which are the Al–O bond lengths calculated from the bond valence method.[56] The position of the peak for sixfold coordinated aluminum atoms was set at the average Al–O bond length of 1.86 Å found from the powder diffraction work (Table V). The width of the Gaussian peak describing AlO$_4$ units was set at 0.05 Å, which is a typical value for AlO$_4$ units in alumino–phosphate glasses,[50] and the width of the Gaussian peak describing AlO$_6$ units was set at 0.07 Å, which is representative of the value found in the crystalline NAGP materials with $x = 0.4$ and $x = 0.8$ (Table S2). The width of the Gaussian peak describing AlO$_5$ units was set in between these values at 0.06 Å. Additional peaks at larger-r values were used in order to constrain the fitted functions at lower r.

For the as-prepared glasses with $x = 0.4$ and $x = 0.8$, the fitted GEM $D'(r)$ functions are shown in Figs. 17(b) and 18(b), respectively, and the fitted P–O and Ge–O peak parameters are summarized in Table S5. The results provided starting parameters for fitting the D4c datasets for the as-prepared glasses. The fitted D4c $D'(r)$ functions for the $x = 0.4$ and $x = 0.8$ compositions are shown in Figs. 21(b) and 22(b), respectively, and the

fitted peak parameters are summarized in Table S7. The fitted XRD $D'(r)$ functions for the as-prepared glasses with $x = 0.4$ and $x = 0.8$ are shown in Figs. 19(b) and 20(b), respectively, and the fitted P–O and Ge–O peak parameters are summarized in Table S6. The results give a P–O coordination number of $\bar{n}_P^O = 4$ within the experimental error and indicate a reduction in the average Ge–O coordination number as more aluminum is added to the glass structure.

The XRD and D4c results obtained for the as-prepared glasses provided starting parameters for fitting the datasets for the annealed glasses, where the aluminum speciation was taken from ^{27}Al MAS NMR experiments (Table VII). The fitted XRD $D'(r)$ functions for the $x = 0.4$ and $x = 0.8$ compositions are shown in Figs. 19(c) and 20(c), respectively, and the fitted P–O and Ge–O peak parameters are summarized in Table S8. The fitted D4c $D'(r)$ functions for the $x = 0.4$ and $x = 0.8$ compositions are shown in Figs. 21(c) and 22(c), respectively, and the fitted P–O and Ge–O peak parameters are summarized in Table S9. The results do not show a change to $\bar{n}_P^O$ but, for each composition, indicate an increase in $\bar{n}_{Ge}^O$ relative to the as-prepared glass.
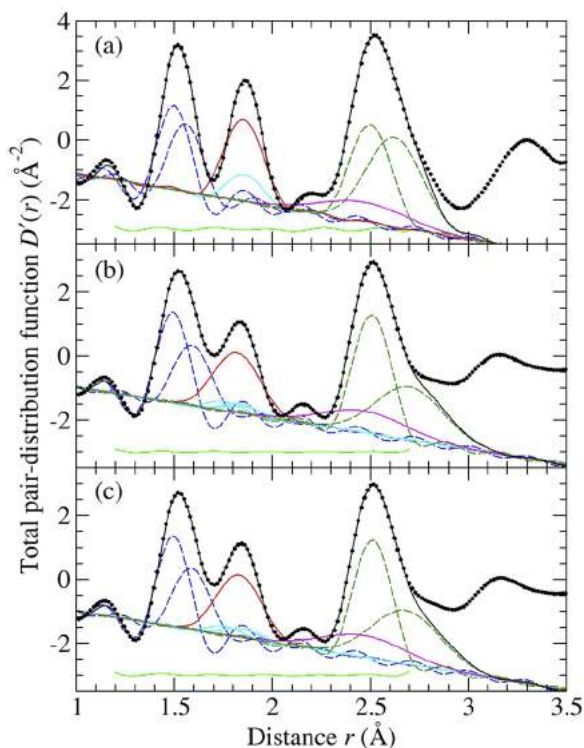
FIG. 22. The fitted $D'(r)$ functions for (a) crystalline, (b) as-prepared glassy, and (c) annealed glassy NAGP with $x = 0.8$ measured using D4c. The filled circles give the measured function; the black solid curve gives the fitted function; and the other curves show the contributions from the P–O (blue broken curves), Al–O (cyan solid curves), Ge–O (red solid curve), Na–O (magenta solid curve), and O–O (green broken curves) correlations. The displaced green solid curve shows the residual. For the glass, the Na–O and O–O correlations are introduced to constrain the peaks fitted at smaller r-values.

V. DISCUSSION

A. Crystal vs glass structure

The P–O and Ge–O bond distances and coordination numbers obtained from the ND and XRD pair-distribution function analyses are summarized in Table VIII. The diffraction results for the glasses show Ge–O coordination numbers that are markedly smaller than $\bar{n}_{Ge}^{O} = 6$, which indicates the presence of polyhedral GeO_5 and/or GeO_4 units. This observation of a substantial difference between the crystal and glass structures is supported by solid-state NMR experiments.[12] For example, the ^{31}P chemical shifts differ by more than 10 ppm; P–O–P linkages are absent in the crystal but may be present at low concentrations in the glass; and $P^{(3)}$ phosphate units dominate the structure of the glasses but are absent in the isochemical crystals where all the phosphate units are $P^{(4)}$. In the case of NAGP with $x = 0$, ^{23}Na spin-echo decay spectroscopy finds that the second moment quantifying the strength of Na–Na interactions is about twice as large in the glass as compared to the isochemical crystal, which suggests that some Na–Na distances are shorter in the glass than in the crystal. Furthermore, Al is exclusively six-coordinated

in the aliovalently (Al + Na) substituted crystalline materials but is found in a mixture of fourfold, fivefold, and sixfold coordination environments in the glass (Table VII).

B. Structural model for M_2O–Al_2O_3–GeO_2–P_2O_5 materials

In order to investigate the network connectivity via the BO vs non-bridging oxygen (NBO) content of the NAGP materials, it is instructive to consider a simple model based on the oxygen coordination number.[48] Let us assume that all oxygen atoms are part of a network and occupy either NBO or BO sites with coordination numbers of one or two, respectively. Then, the fraction of NBO atoms is given by

$$f_{NBO} = N_{NBO}/N_O = 2 - \bar{n}_O^P - \bar{n}_O^{Ge} - \bar{n}_O^{Al}, \quad (10)$$

where N_{NBO} is the number of NBO atoms and N_O is the total number of oxygen atoms. For a fully polymerized network, $\bar{n}_O^P + \bar{n}_O^{Ge} + \bar{n}_O^{Al} = 2$ and $f_{NBO} = 0$. For a fully depolymerized network, $\bar{n}_O^P + \bar{n}_O^{Ge} + \bar{n}_O^{Al} = 1$ and $f_{NBO} = 1$. The model does not allow for the formation of threefold coordinated oxygen atoms as supported, for example, by ^{17}O NMR experiments on GeO_2–P_2O_5 glass.[64] The number of O-β bonds between oxygen and atoms of chemical species β is equal to the number of β-O bonds, i.e., $N_O \bar{n}_O^{\beta} = N_\beta \bar{n}_\beta^O$, where N_β is the number of β atoms, such that $c_O \bar{n}_O^{\beta} = c_\beta \bar{n}_\beta^O$. Hence, the fraction of NBO atoms can be re-written as

$$f_{NBO} = \left(2c_O - c_P \bar{n}_P^O - c_{Ge} \bar{n}_{Ge}^O - c_{Al} \bar{n}_{Al}^O\right)/c_O. \quad (11)$$

In the following, it will be assumed that all the nearest-neighbor oxygen atoms to Ge and Al are BO atoms, in accordance with the crystal structures where each of these oxygen atoms is shared with a phosphorus atom. The number of NBO atoms per phosphorus atom is given by $N_{NBO}/N_P = (c_O/c_P)f_{NBO}$, where N_P is the number of phosphorus atoms. Hence, if the P–O coordination number $\bar{n}_P^O = 4$ and NBO atoms reside on phosphorus atoms alone, the number of BO atoms per phosphorus atom

$$N_{BO}/N_P = 4 - (c_O/c_P)f_{NBO}. \quad (12)$$

In the case of glassy $(GeO_2)_x(NaPO_3)_{1-x}$, for example, O-1s x-ray photoemission spectroscopy (XPS) experiments indicate that most of the NBO atoms are bound to P and not Ge, e.g., 100% for $x = 0$ vs 82.5% for $x = 0.5$.[65] For M_2O–P_2O_5 materials, Eq. (12) will also give the nearest-neighbor P–P coordination number $\bar{n}_P^P$. The number of NBO atoms per M atom $N_{NBO}/N_M = (c_O/c_M)f_{NBO}$, where N_M is the number of M atoms. The number of BO atoms per M atom $N_{BO}/N_M = (c_O/c_M)(1 - f_{NBO})$.

The nearest-neighbor O–O coordination number is given by

$$\bar{n}_O^O = f_{NBO}\bar{n}_{NBO}^O + f_{BO}\bar{n}_{BO}^O, \quad (13)$$

where the fraction of BO atoms $f_{BO} = 1 - f_{NBO}$. The coordination numbers $\bar{n}_{BO}^O$ and $\bar{n}_{NBO}^O$ for the BO and NBO atoms will depend on

TABLE VIII. The mean P–O and Ge–O bond distances and coordination numbers obtained from Gaussian peak fits to the r-space functions measured using ND and XRD for the as-prepared and annealed NAGP glasses and corresponding crystalline phases. The shorter and longer P–O bond distances, obtained by representing the nearest-neighbor P–O correlations by two Gaussian functions, are distinguished.

x	Material	r_{PO}(short) (Å)	r_{PO}(long) (Å)	$\bar{n}_P^O$ (sum)	r_{GeO} (Å)	$\bar{n}_{Ge}^O$
0.0	Glass: As-prepared	1.513(13)	1.573(15)	3.97(3)	1.826(2)	5.07(7)
	Glass: Annealed[a]	1.512(17)	1.568(26)	3.97(4)	1.831(1)	5.11(2)
	Glass: Annealed[b]	1.498(4)	1.584(5)	3.99(3)	1.831(5)	5.09(5)
	Glass: Annealed[c]	1.491(4)	1.588(5)	3.99(3)	1.835(5)	5.21(5)
	Crystal	1.517(10)	1.546(10)	3.93(5)	1.858(1)	5.94(3)
0.4	Glass: As-prepared	1.509(15)	1.568(19)	3.99(1)	1.826(2)	4.93(8)
	Glass: Annealed	1.507(18)	1.572(17)	3.95(5)	1.831(1)	5.07(12)
	Crystal	1.513(14)	1.545(13)	3.93(7)	1.861(2)	6.02(3)
0.8	Glass: As-prepared	1.510(12)	1.571(15)	3.96(4)	1.824(4)	4.84(12)
	Glass: Annealed	1.509(14)	1.571(18)	3.95(5)	1.833(2)	4.97(15)
	Crystal	1.512(10)	1.546(8)	3.98(5)	1.857(3)	6.03(4)

[a] T_{TT} = 873 K for 0.25 h.
[b] T_{TT} = 876 K for 0.25 h.
[c] T_{TT} = 876 K for 0.5 h.

the network connectivity. For example, the structure of crystalline NAGP with $x = 0$ is based on a network of corner-sharing tetrahedral PO_4 and octahedral GeO_6 units in which each BO atom is shared between a tetrahedron and an octahedron. Each BO atom therefore has three nearest-neighbor O atoms within a tetrahedron and four nearest-neighbor O atoms within an octahedron such that $\bar{n}_O^O = \bar{n}_{BO}^O = 7$.

The parameters predicted by the structural model for a variety of crystalline $M_2O–Al_2O_3–GeO_2–P_2O_5$ materials (Table IX) match the measured values. For the cases of crystalline NAGP[2,43] and LAGP,[63] the Al^{3+} ions substitute at the sites of the Ge^{4+} ions such that $\bar{n}_{Al}^O = \bar{n}_{Ge}^O = 6$, so there is no change to N_{NBO}/N_P or N_{NBO}/N_M and $f_{NBO} = 0$. By contrast, in glassy NAGP, the Ge–O and Al–O coordination numbers take values smaller than 6, so NBO atoms appear. The fraction of NBO atoms increases as the composition is changed from $x = 0$ to $x = 0.8$, leading to an increase in N_{NBO}/N_P

and a decrease in N_{NBO}/N_{Na} [Figs. 23(c)–23(e)]. The N_{NBO}/N_P ratios are consistent with a mixture of $P^{(3)}$ and $P^{(4)}$ species, as found from ^{31}P solid-state NMR experiments (Sec. IV B). If all the phosphate groups are either $P^{(3)}$ or $P^{(4)}$, it follows that the fraction of $P^{(3)}$ species for the as-prepared glass is 0.618(44) at $x = 0$ vs 0.770(52) at $x = 0.8$. The annealing procedure leads to a reduction in f_{NBO} for each of the glasses, corresponding to a small increase in the Ge–O and Al–O coordination numbers, which leads to a decrease in both N_{NBO}/N_P and N_{NBO}/N_{Na}.
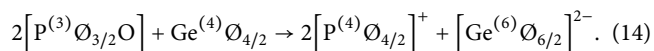
C. Super-structural units

A challenge is to provide a structural model for NAGP glasses in which the phosphate species are constrained to be either $P^{(3)}$ or $P^{(4)}$ and the mean Ge–O and Al–O coordination numbers are both substantially larger than four. A starting point is provided by the model of Ren and Eckert[66] for sodium phosphosilicate glasses, which invokes super-structural units containing sixfold coordinated silicon atoms (Fig. 24). For simplicity, the focus in the following will be on the NAGP glass with $x = 0$. BO atoms will be denoted by Ø, and as mentioned before, the number of BO atoms per Ge or P atom will be denoted by a superscript.

The NAGP glass composition for $x = 0$ can be written as $(Na_2P_6GeO_{18})_{1/2}(GeO_2)_{3/2}$. In the model of Ren and Eckert, the $Na_2P_6GeO_{18}$ part of the glass is built from $[Ge^{(6)}P_6^{(3)}Ø_{10}Ø_{4/2}O_6]^{2-}$ super-structural units, where the negative charge on a unit is compensated by two Na^+ ions, and the GeO_2 part of the glass is built from charge-neutral corner-sharing tetrahedral $Ge^{(4)}$ units. The model therefore contains only $P^{(3)}$, $Ge^{(4)}$, and $Ge^{(6)}$ species. All NBO atoms reside within the $P^{(3)}$ motifs of a super-structural unit, where charge-shuttling ensures that they carry a partial charge of $-(2/6)e = -0.33e$ and e is the elementary charge. The model delivers a coordination number $\bar{n}_{Ge}^O = 4.5$ for NAGP glass with $x = 0$, which is smaller than the value found from the diffraction experiments (Table VIII).

TABLE IX. The parameters predicted by the structural model of Sec. V B using $\bar{n}_P^O = 4$ and the reported values of $\bar{n}_{Ge}^O$ and $\bar{n}_{Al}^O$ for several crystalline $M_2O–Al_2O_3–GeO_2–P_2O_5$ materials.

Material	$\bar{n}_{Ge}^O$	$\bar{n}_{Al}^O$	f_{NBO}	N_{NBO}/N_P	N_{BO}/N_P	N_{NBO}/N_M	References
P_2O_5	⋯	⋯	0.4	1	3	⋯	57
$NaPO_3$	⋯	⋯	2/3	2	2	2	58
Na_3PO_4	⋯	⋯	1	4	0	4/3	59
GeP_2O_7	6	⋯	0	0	4	⋯	60
$KGeOPO_4$	6	⋯	0	0	4	0	61
$Cs_2GeP_4O_{13}$	6	⋯	0.307 69	1	3	2	2
$KGe_2(PO_4)_3$	6	⋯	0	0	4	0	62
NAGP[a]	6	6	0	0	4	0	2 and 43
LAGP[b]	6	6	0	0	4	0	63

[a] $x = 0$ or 0.127.
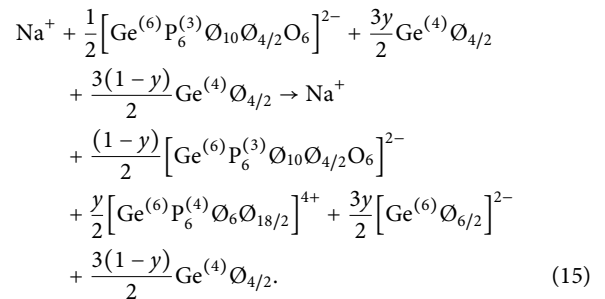[b] $x = 0, 0.24, 0.40, 0.44, 0.47,$ or 0.48.

FIG. 23. Composition dependence of the (a) electrical conductivity σ at 573 K and (b) activation energy E_a in crystalline vs as-prepared glassy NAGP.[4,8] (c)–(e) Several of the parameters describing the NBO atoms in as-prepared vs annealed NAGP glasses. In (a) and (b), the crystalline materials were obtained from the as-prepared glass either (i) by thermal annealing at a temperature in the range 917–939 K for 3 h (Ortiz-Mosquera et al.[8]) or (ii) by a two stage process in which crystals were first nucleated by heating for 2 h at a temperature between T_g = 851 K and T_x = 937 K and the resultant material was then annealed at 1023 K for 18 h (Zhang et al.[4]). In (a), the results for the glass are scaled by a factor of 27. In (b), the error bars are smaller than the symbol size. In (c)–(e), the parameters were obtained from the structural model of Sec. V B using $\bar{n}_P^O$ = 4, the $\bar{n}_{Al}^O$ values from ^{27}Al MAS NMR, and the average $\bar{n}_{Ge}^O$ values from diffraction. For the x = 0 composition, the annealed glass corresponds to T_{TT} = 873 K.

A larger coordination number can be obtained, however, by using the NBO atoms within the $P^{(3)}$ motifs of a super-structural unit to convert $Ge^{(4)}$ to $Ge^{(6)}$ units according to the following scheme:

$$2\left[P^{(3)}\emptyset_{3/2}O\right] + Ge^{(4)}\emptyset_{4/2} \rightarrow 2\left[P^{(4)}\emptyset_{4/2}\right]^+ + \left[Ge^{(6)}\emptyset_{6/2}\right]^{2-}. \quad (14)$$

In the crystal structures (Sec. IV A), $P^{(4)}$–$\emptyset$–$P^{(4)}$ linkages are absent, i.e., the phosphate chains in the model of Ren and Eckert must dissociate as $Ge^{(6)}$ species join to expand a super-structural unit. It is therefore proposed that a proportion y of the initial super-structural

units are converted to $[Ge^{(6)}P_6^{(4)}\emptyset_6\emptyset_{18/2}]^{4+}$ units according to the following scheme:

$$Na^+ + \frac{1}{2}\left[Ge^{(6)}P_6^{(3)}\emptyset_{10}\emptyset_{4/2}O_6\right]^{2-} + \frac{3y}{2}Ge^{(4)}\emptyset_{4/2}$$

$$+ \frac{3(1-y)}{2}Ge^{(4)}\emptyset_{4/2} \rightarrow Na^+$$

$$+ \frac{(1-y)}{2}\left[Ge^{(6)}P_6^{(3)}\emptyset_{10}\emptyset_{4/2}O_6\right]^{2-}$$

$$+ \frac{y}{2}\left[Ge^{(6)}P_6^{(4)}\emptyset_6\emptyset_{18/2}\right]^{4+} + \frac{3y}{2}\left[Ge^{(6)}\emptyset_{6/2}\right]^{2-}$$

$$+ \frac{3(1-y)}{2}Ge^{(4)}\emptyset_{4/2}. \quad (15)$$

In each of the new $[Ge^{(6)}P_6^{(4)}\emptyset_6\emptyset_{18/2}]^{4+}$ units, there are no internal $P^{(4)}$–$\emptyset$–$P^{(4)}$ linkages, i.e., each of the six $P^{(4)}$ motifs has three BO atoms that form external connections.

Now, $\bar{n}_{Ge}^O = 4f_{Ge}^{(4)} + 6f_{Ge}^{(6)}$, where $f_{Ge}^{(i)}$ is the fraction of $Ge^{(i)}$ atoms, and $f_{Ge}^{(4)} + f_{Ge}^{(6)} = 1$. The revised model of Eq. (15) gives $f_{Ge}^{(6)} = (1 + 3y)/4$, so it follows that $\bar{n}_{Ge}^O = 3(y + 3)/2$. The fraction of NBO atoms is given by

$$f_{NBO} = (1 - y)/4 \quad (16)$$

and $f_{NBO} + f_{BO} = 1$. All the phosphate motifs are either $P^{(3)}$ or $P^{(4)}$, where $P^{(3)}$ has one NBO atom and $P^{(4)}$ has only BO atoms, so

$$f_P^{(3)} = N_{NBO}/N_P = (1 - y), \quad (17)$$

$f_P^{(3)} + f_P^{(4)} = 1$, and $N_{NBO}/N_P + N_{BO}/N_P = 4$. The $P^{(4)}$ motifs carry a formal charge of $+e$, so they will interact more weakly with Na^+ ions than the $P^{(3)}$ motifs, which offers a route to distinguishing between these phosphate units by using solid-state NMR (Sec. IV B). The number of NBO atoms per sodium atom

$$N_{NBO}/N_{Na} = 3(1 - y) \quad (18)$$

and $N_{NBO}/N_{Na} + N_{BO}/N_{Na} = 12$. All these equations are in accord with those found in Sec. V B, which were derived on the basis of a maximum oxygen coordination number of 2.

In the y = 1 limit, $\bar{n}_{Ge}^O$ = 6 and f_{NBO} = 0 such that $f_P^{(4)}$ = 1, as found for crystalline NAGP with x = 0 (Sec. IV A). Hence, each $Ge^{(6)}$ motif will be connected to six $P^{(4)}$ motifs within a super-structural unit and the $[Ge^{(6)}P_6^{(4)}\emptyset_6\emptyset_{18/2}]^{4+}$:$[Ge^{(6)}\emptyset_{6/2}]^{2-}$ ratio of 1:3 means that each $P^{(4)}$ motif can be connected to four $Ge^{(6)}$ motifs. The model thereby enables the strict $P^{(4)}$–$\emptyset$–$Ge^{(6)}$–$\emptyset$–$P^{(4)}$ and $Ge^{(6)}$–$\emptyset$–$P^{(4)}$–$\emptyset$–$Ge^{(6)}$ connectivity found in the crystal structure.

For NAGP with x = 0, the parameters predicted by the super-structural model on the basis of the measured Ge–O coordination numbers are summarized in Table X. The results indicate that super-structural units can grow on thermal annealing by converting $P^{(3)}$ to $P^{(4)}$ motifs in order to accommodate more $Ge^{(6)}$ units, i.e., the super-structural units provide the nucleation sites for crystal growth via a homogeneous nucleation mechanism (Sec. I).

In accord with the solid-state NMR results of Sec. IV B, the model predicts that $P^{(3)}$ units are in the majority in the glass and
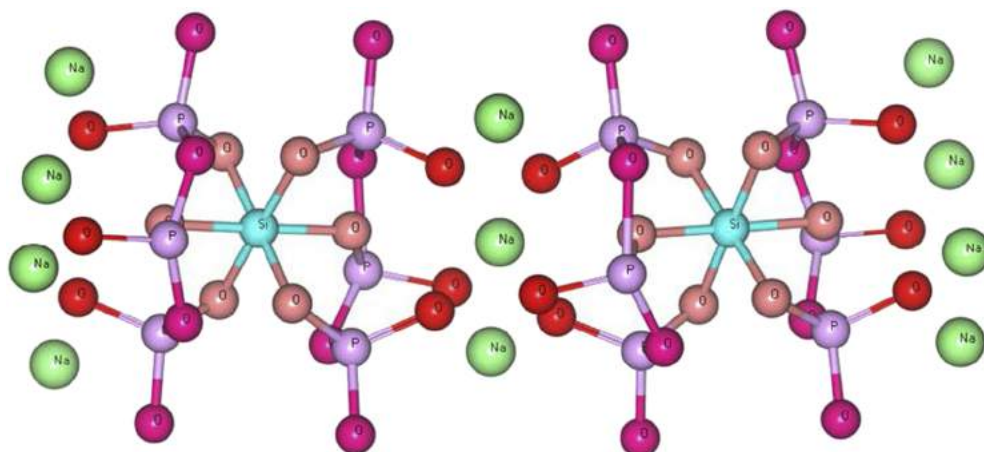
FIG. 24. Two of the $[Si^{(6)}P_6^{(3)}\emptyset_{10}\emptyset_{4/2}O_6]^{2-}$ super-structural units in the model of Ren and Eckert[66] for glassy $Na_2P_6SiO_{18}$, where charge-shuttling ensures that the NBO atoms in the $P^{(3)}$ phosphate motifs carry a partial negative charge. Other super-structural units (not shown) ensure that the top and bottom rows of Na^+ ions have a 1/4 share in each unit and that the remaining Na^+ ions have a 1/2 share in each unit. The charge of $-4e$ on the illustrated units is therefore balanced by the net charge of $(5e \times 1/2) + (6e \times 1/4) = +4e$ on the illustrated Na^+ ions. Reprinted with permission from J. Ren and H. Eckert, J. Phys. Chem. C **122**, 27620 (2018). Copyright 2018, American Chemical Society.

interact more strongly with sodium ions than $P^{(4)}$ units, which carry a formal positive charge. The model also predicts that $P^{(3)}$ units are replaced by $P^{(4)}$ units as crystallization progresses, a finding that is also supported by the solid-state NMR results (Table X). In the analogous $LiGe_2(PO_4)_3$ system, Raman spectra for the glass show a band attributed to $P^{(3)}$ phosphate species near 1280 cm^{-1}, which is not found in the crystalline phase where all the phosphate species are $P^{(4)}$.[67]

D. Model development

In the original model of Ren and Eckert,[66] which corresponds to $y = 0$ in Sec. V C, the $Ge^{(4)}:Ge^{(6)}$ ratio is 3:1 and $\bar{n}_{Ge}^O = 4.5$. For simplicity, the adapted model does not invoke $Ge^{(5)}$ units although it does give a mean Ge–O coordination number $\bar{n}_{Ge}^O = 5$ if there are equal numbers of $Ge^{(4)}$ and $Ge^{(6)}$ units ($y = 1/3$). The additional $Ge^{(6)}$ units form bridges between the super-structural motifs via $P^{(4)}–\emptyset–Ge^{(6)}–\emptyset–P^{(4)}$ connections.

Fivefold coordinated germanium atoms may, nevertheless, exist. For example, since Ge and Al atoms can be substituted for one another in the crystalline NAGP materials, this possibility also exists for the NAGP glasses where Al(V) species are observed in the

^{27}Al MAS NMR experiments (Table VII). Indeed, the mean coordination numbers $\bar{n}_{Al}^O$ and $\bar{n}_{Ge}^O$ take similar values for each of the as-prepared glasses, and both values increase when the material is thermally annealed (Table XI).

$Ge^{(5)}$ units could be introduced into the model for the glass via a scenario in which a germanium atom in the GeO_2 part of the glass accepts the NBO atom of only one $P^{(3)}$ unit, which would lead to a new $P^{(4)}–\emptyset–Ge^{(5)}$ connectivity linking the super-structural unit to the GeO_2 part of the glass. Unfortunately, neither diffraction nor the deduction from the NMR results can give more than an average coordination number for the Ge atoms. As a matter of fact, none of the available structural techniques have been able to unambiguously identify distinct $Ge^{(5)}$ units in germanate glasses. Fivefold coordinated germanium atoms, along with threefold coordinated oxygen atoms, could also be introduced into the model for the glass by enabling their presence in the GeO_2 part of the network structure.

In its simplest form, the super-structural model of Sec. V C could be extended to aluminum containing glasses by treating the Ge and Al atoms as equivalent and introducing sodium to charge compensate. A more realistic model would benefit from knowledge of the $P^{(3)}$ and $P^{(4)}$ nearest-neighbors. For example, each $P^{(3)}$ unit

TABLE X. Parameters predicted for the $x = 0$ composition by the model of Sec. V C and the ratio $f_P^{(3)}/f_P^{(4)}$ measured in the ^{31}P MAS NMR experiments. The $\bar{n}_{Ge}^O$ values are taken from Table VIII, and the NMR results are taken from Table VI.

Material	$\bar{n}_{Ge}^O$	y	f_{NBO}	N_{NBO}/N_{Na}	$f_P^{(3)}/f_P^{(4)}$	$f_P^{(3)}/f_P^{(4)}$ (NMR)
Glass: As-prepared	5.07(7)	0.382(44)	0.154(11)	1.85(13)	1.62(22)	2.13(6)
Glass: Annealed at T_{TT} = 873 K for 0.25 h	5.11(2)	0.407(13)	0.148(3)	1.78(4)	1.46(6)	1.70(5)
Glass: Annealed at T_{TT} = 876 K for 0.25 h	5.09(5)	0.393(33)	0.152(8)	1.82(10)	1.54(16)	1.56(4)
Glass: Annealed at T_{TT} = 876 K for 0.5 h	5.21(5)	0.473(33)	0.132(8)	1.58(10)	1.11(11)	0.96(3)

TABLE XI. The Al–O and Ge–O coordination numbers for the NAGP glasses with $x = 0.4$ and $x = 0.8$ found from the ^{27}Al MAS NMR (Table VII) and diffraction (Table VIII) experiments.

x	Material	$\bar{n}_{Al}^{O}$	$\bar{n}_{Ge}^{O}$
0.4	Glass: As-prepared	4.86(6)	4.93(8)
	Glass: Annealed	4.96(6)	5.07(12)
0.8	Glass: As-prepared	4.85(6)	4.84(12)
	Glass: Annealed	4.94(6)	4.97(15)

comprises at least three different subtypes, depending on whether the BO atoms are connected to three Ge, two Ge and one Al, or one Ge and two Al atoms (the environment with three Al atoms will have a negligible statistical probability). In principle, one could try to identify these neighbors with the help of ^{31}P{^{23}Na} REAPDOR in combination with ^{31}P{^{27}Al} REAPDOR experiments, but the analysis will be complicated.

E. Ion transport

The electrical conductivity in electrolytes with the NASICON structure is considered to be predominantly ionic, with an ion transport number approaching unity.[68] For these materials, in which the electrical conduction originates from the migration of a single charge carrier species, the ionic conductivity is given by $\sigma = ne\mu$, where n is the effective carrier concentration, e is the charge on the mobile Na$^+$ ions, and μ is the ion mobility. In the case of polycrystalline materials, there will be contributions to this conductivity from ion transport both in grains and at grain boundaries. A contribution from grain boundaries will not feature in conductivity measurements on glass, provided that the samples are unpowdered.

In crystalline NAGP, the electrical conductivity increases by almost two orders of magnitude and the activation energy E_a for the conductivity decreases as the composition is changed from $x = 0$ to $x = 0.8$ [Figs. 23(a) and 23(b)], i.e., as Ge^{4+} ions are aliovalently substituted by Al^{3+} ions and additional Na$^+$ ions are introduced to compensate for the charge deficit. This substitution does not generate NBO atoms, i.e., in the absence of coordination defects, $f_{NBO} = 0$ across the composition range. The conductivity is between 3.2 and 40 times larger than that of the isochemical as-prepared glass.[8]

For the glass, the composition dependence of σ for the crystalline materials can be roughly matched by scaling [Fig. 23(a)]. The conductivity of the glass also increases with the concentration of Na$^+$ ions, but the mobility of these ions is smaller in the more disordered glass structure. NBO atoms are present in the glass as part of the P$^{(3)}$ motifs on the super-structural units (Sec. V C). They are negatively polarized and presumably influence the Na$^+$ ion mobility, although the role that they play is unclear. While it has been suggested that NBO atoms at the P$^{(2)}$ sites in phosphate glasses can act as local traps for Na$^+$ ions,[69] the traps generated by NBO atoms at the P$^{(3)}$ sites of the super-structural units carry only a fractional negative charge and are thus expected to be significantly more shallow.

VI. CONCLUSIONS

The structure of crystalline NAGP with $x = 0$, 0.4, and 0.8 was investigated using neutron and x-ray powder diffraction and pair-distribution function analysis. The latter indicates deformable tetrahedral PO$_4$ units in that the distribution of P–O distances is broader than can be accommodated by using a single Gaussian peak to describe the nearest-neighbor P–O correlations. The ionic conductivity increases with x as more Na$^+$ ions are introduced. The ion transport does not involve NBO atoms because they are absent from the crystal structures.

The structure of the corresponding glasses was investigated by neutron and x-ray pair-distribution function analysis and solid-state NMR spectroscopy. There is a substantial reduction in the Ge–O and Al–O coordination numbers from the value $\bar{n}_{Ge}^{O} = \bar{n}_{Al}^{O} = 6$ found in the crystalline phases, which leads to the creation of NBO atoms. The fraction of these atoms f_{NBO} is quantified via a structural model based on the oxygen coordination number. The ionic conductivity of the glass increases with the concentration of Na$^+$ ions, an enhancement that is accompanied by an increase in both f_{NBO} and the ratio NBO:P vs a decrease in the ratio NBO:Na. The effect of NBO atoms on the Na$^+$ ion mobility is in need of further investigation.

A structural model is proposed for the $x = 0$ glass by adapting the model of Ren and Eckert[66] for phosphosilicate glasses. Here, the super-structural units of this model can be modified by using the donor function of a doubly bonded NBO atom on a P$^{(3)}$ motif to convert Ge$^{(4)}$ atoms to higher-coordinated germanium atoms, thereby converting P$^{(3)}$ to P$^{(4)}$ motifs and increasing the size of a super-structural unit. The P$^{(4)}$ species have a formal positive charge so that they do not attract sodium ions. Accordingly, they interact more weakly with Na$^+$ ions than the P$^{(3)}$ species. Justification for the structural model is provided by deconvolution of the ^{31}P MAS NMR spectra for the as-prepared glass that is consistent with the ^{31}P{^{23}Na} REAPDOR results.

When the as-prepared glass is thermally annealed, the ^{31}P MAS NMR spectra show an increase in the fraction of P$^{(4)}$ species, indicating a further progression to the super-structural modification process. This modification is also seen by a moderate increase in the Ge–O coordination number found from the diffraction experiments and a concomitant reduction in f_{NBO}. The P$^{(4)}$ species generated within the modified super-structural units by the reaction between P$^{(3)}$ and Ge$^{(4)}$ motifs therefore provide the nucleation sites for crystal growth via a homogeneous nucleation mechanism.

SUPPLEMENTARY MATERIAL

See the supplementary material for Fig. S1 that gives a more detailed comparison of the ^{31}P MAS NMR spectra shown in Fig. 5 for the as-prepared glass and the glass annealed at $T_{TT} = 873$ K for 0.25 h. Figure S2 shows the fitted $D'(r)$ functions measured using D4c for the NAGP samples with $x = 0$ annealed at $T_{TT} = 876$ K for either 0.25 or 0.5 h. Table S1 lists the parameters obtained from the fits to the ^{27}Al MAS NMR spectra shown in Fig. 8. Tables S2–S9 list the parameters obtained from the fits to the real-space functions measured by ND or XRD that are shown in Figs. 14–22 and Fig. S2.

DATA AVAILABILITY

The data that support the findings of this study are openly available in the University of Bath Research Data Archive at https://doi.org/10.15125/BATH-00980.[70] Further details of the crystal structures are given in Ref. 71. The measured neutron diffraction datasets for the D4c and GEM experiments are available from Refs. 72–74.

REFERENCES

[1] G. H. Beall, Front. Mater. **3**, 37 (2016).
[2] D. Zhao, Z. Xie, J.-M. Hu, H. Zhang, W.-L. Zhang, S.-L. Yang, and W.-D. Cheng, J. Mol. Struct. **922**, 127 (2009).
[3] H. Eckert and A. C. Martins Rodrigues, MRS Bull. **42**, 206 (2017).
[4] Q. Zhang, Z. Wen, Y. Liu, S. Song, and X. Wu, J. Alloys Compd. **479**, 494 (2009).
[5] J. Fu, Solid State Ionics **104**, 191 (1997).
[6] E. D. Zanotto, J. E. Tsuchida, J. F. Schneider, and H. Eckert, Int. Mater. Rev. **60**, 376 (2015).
[7] M. Guin and F. Tietz, J. Power Sources **273**, 1056 (2015).
[8] J. F. Ortiz-Mosquera, A. M. Nieto-Muñoz, and A. C. M. Rodrigues, J. Non-Cryst. Solids **513**, 36 (2019).
[9] A. M. Rodrigues, J. L. Narváez-Semanate, A. A. Cabral, and A. C. M. Rodrigues, Mater. Res. **16**, 811 (2013).
[10] Y. Inda, T. Katoh, and M. Baba, J. Power Sources **174**, 741 (2007).
[11] C. Schröder, J. Ren, A. C. M. Rodrigues, and H. Eckert, J. Phys. Chem. C **118**, 9400 (2014).
[12] H. Bradtmüller, A. M. Nieto-Muñoz, J. F. Ortiz-Mosquera, A. C. M. Rodrigues, and H. Eckert, J. Non-Cryst. Solids **489**, 91 (2018).
[13] H. M. Rietveld, Acta Crystallogr. **22**, 151 (1967).
[14] H. M. Rietveld, J. Appl. Crystallogr. **2**, 65 (1969).
[15] H. E. Fischer, A. C. Barnes, and P. S. Salmon, Rep. Prog. Phys. **69**, 233 (2006).
[16] D. Waasmaier and A. Kirfel, Acta Crystallogr., Sect. A **51**, 416 (1995).
[17] V. F. Sears, Neutron News **3**, 26 (1992).
[18] R. A. Martin, P. S. Salmon, H. E. Fischer, and G. J. Cuello, J. Phys.: Condens. Matter **15**, 8235 (2003).
[19] D. I. Grimley, A. C. Wright, and R. N. Sinclair, J. Non-Cryst. Solids **119**, 49 (1990).
[20] E. Lorch, J. Phys. C: Solid State Phys. **2**, 229 (1969).
[21] P. S. Salmon, J. Phys.: Condens. Matter **18**, 11443 (2006).
[22] A. Franz and A. Hoser, J. Large-Scale Res. Facil. **3**, A103 (2017).
[23] J. Rodríguez-Carvajal, FULLPROF (version 5.30): A program for Rietveld refinement and pattern matching analysis, Insitut Laue-Langevin, Grenoble, France, 2012.
[24] J. Rodríguez-Carvajal, Physica B **192**, 55 (1993).
[25] L. M. Gelato and E. Parthé, J. Appl. Crystallogr. **20**, 139 (1987).
[26] K. Momma and F. Izumi, J. Appl. Crystallogr. **44**, 1272 (2011).
[27] H. E. Fischer, G. J. Cuello, P. Palleau, D. Feltin, A. C. Barnes, Y. S. Badyal, and J. M. Simonson, Appl. Phys. A **74**, s160 (2002).
[28] A. Zeidler, P. S. Salmon, H. E. Fischer, J. C. Neuefeind, J. Mike Simonson, and T. E. Markland, J. Phys.: Condens. Matter **24**, 284126 (2012).
[29] H. Bertagnolli, P. Chieux, and M. D. Zeidler, Mol. Phys. **32**, 759 (1976).
[30] P. S. Salmon, S. Xin, and H. E. Fischer, Phys. Rev. B **58**, 6115 (1998).
[31] A. C. Hannon, Nucl. Instrum. Methods Phys. Res., Sect. A **551**, 88 (2005).
[32] S. E. McLain, D. T. Bowron, A. C. Hannon, and A. K. Soper, "Gudrun: A computer program developed for analysis of neutron diffraction data," Technical Report, ISIS Facility, Rutherford Appleton Laboratory, Chilton, Didcot, Oxon, United Kingdom, 2006.
[33] M. A. Howe, R. L. McGreevy, and W. S. Howells, J. Phys.: Condens. Matter **1**, 3433 (1989).
[34] P. S. Salmon, A. Zeidler, and H. E. Fischer, J. Appl. Crystallogr. **49**, 2249 (2016).
[35] A. P. Hammersley, J. Appl. Crystallogr. **49**, 646 (2016).
[36] X. Qiu, J. W. Thompson, and S. J. L. Billinge, J. Appl. Crystallogr. **37**, 678 (2004).
[37] J.-B. d'Espinose de Lacaillerie, C. Fretigny, and D. Massiot, J. Magn. Reson. **192**, 244 (2008).
[38] D. Massiot, F. Fayon, M. Capron, I. King, S. Le Calvé, B. Alonso, J.-O. Durand, B. Bujoli, Z. Gan, and G. Hoatson, Magn. Reson. Chem. **40**, 70 (2002).
[39] T. Gullion and J. Schaefer, J. Magn. Reson. **81**, 196 (1989).
[40] T. Gullion, Chem. Phys. Lett. **246**, 325 (1995).
[41] L.-O. Hagman and P. Kierkegaard, Acta Chem. Scand. **22**, 1822 (1968).
[42] M. Carrasco, M. Guillem, and J. Alamo, Solid State Ionics **63-65**, 684 (1993).
[43] P. Maldonado-Manso, M. A. G. Aranda, S. Bruque, J. Sanz, and E. R. Losilla, Solid State Ionics **176**, 1613 (2005).
[44] W. I. F. David, J. Res. Natl. Inst. Stand. Technol. **109**, 107 (2004).
[45] R. D. Shannon, Acta Crystallogr., Sect. A **32**, 751 (1976).

[46]M. Bertmer and H. Eckert, Solid State Nucl. Magn. Reson. **15**, 139 (1999).

[47]J. H. Van Vleck, Phys. Rev. **74**, 1168 (1948).

[48]U. Hoppe, N. P. Wyckoff, R. K. Brow, M. von Zimmermann, and A. C. Hannon, J. Non-Cryst. Solids **390**, 59 (2014).

[49]W. Hoffbauer, S. Wefing, G. Klösters, F. Frick, and M. Jansen, Solid State Nucl. Magn. Reson. **14**, 211 (1999).

[50]R. A. Martin, P. S. Salmon, D. L. Carroll, M. E. Smith, and A. C. Hannon, J. Phys.: Condens. Matter **20**, 115204 (2008).

[51]U. Patel, R. M. Moss, K. M. Z. Hossain, A. R. Kennedy, E. R. Barney, I. Ahmed, and A. C. Hannon, Acta Biomater. **60**, 109 (2017).

[52]A. C. Hannon, in Modern Glass Characterization, edited by M. Affatigato (Wiley, New York, 2015), Chap. 5, pp. 158–240.

[53]G. E. Bacon and R. S. Pease, Proc. R. Soc. London, Ser. A **220**, 397 (1953).

[54]M. K. Wilkinson, E. O. Wollan, and W. C. Koehler, Annu. Rev. Nucl. Sci. **11**, 303 (1961).

[55]L. Koester, K. Knopf, and W. Waschkowski, Z. Phys. A **277**, 77 (1976).

[56]N. E. Brese and M. O'Keeffe, Acta Crystallogr., Sect. B **47**, 192 (1991).

[57]E. H. Arbib, B. Elouadi, J. P. Chaminade, and J. Darriet, J. Solid State Chem. **127**, 350 (1996).

[58]A. McAdam, K. H. Jost, and B. Beagley, Acta Crystallogr., Sect. B **24**, 1621 (1968).

[59]R. J. Harrison, A. Putnis, and W. Kockelmann, Phys. Chem. Chem. Phys. **4**, 3252 (2002).

[60]U. Kaiser and R. Glaum, Z. Anorg. Allg. Chem. **620**, 1755 (1994).

[61]V. I. Voronkova, V. K. Yanovskii, N. I. Sorokina, I. A. Verin, and V. I. Simonov, Kristallografiya **38**, 147 (1993).

[62]R. Brochu, M. Louër, M. Alami, M. Alqaraoui, and D. Louër, Mater. Res. Bull. **32**, 113 (1997).

[63]M. Weiss, D. A. Weber, A. Senyshyn, J. Janek, and W. G. Zeier, ACS Appl. Mater. Interfaces **10**, 10935 (2018).

[64]J. W. Zwanziger, J. L. Shaw, U. Werner-Zwanziger, and B. G. Aitken, J. Phys. Chem. B **110**, 20123 (2006).

[65]J. Ren and H. Eckert, J. Phys. Chem. C **116**, 12747 (2012).

[66]J. Ren and H. Eckert, J. Phys. Chem. C **122**, 27620 (2018).

[67]S. H. Santagneli, H. V. A. Baldacim, S. J. L. Ribeiro, S. Kundu, A. C. M. Rodrigues, C. Doerenkamp, and H. Eckert, J. Phys. Chem. C **120**, 14556 (2016).

[68]S. V. Pershina, B. D. Antonov, A. S. Farlenkov, and E. G. Vovkotrub, J. Alloys Compd. **835**, 155281 (2020).

[69]T. Uchino and Y. Ogata, J. Non-Cryst. Solids **181**, 175 (1995).

[70]P. S. Salmon and A. Zeidler, Data sets for structure of crystalline and amorphous materials in the NASICON system $Na_{1+x}Al_xGe_{2-x}(PO_4)_3$, University of Bath Research Data Archive, 2021, https://doi.org/10.15125/BATH-00980.

[71]Further details of the crystal structure investigations can be obtained from the joint CCDC/FIZ Karlsruhe online deposition service (https://www.ccdc.cam.ac.uk/structures/?) by quoting the deposition numbers CSD: 2059951-2059953. The structural data can be obtained from the crystallography open database (COD, http://www.crystallography.net/cod/) by quoting the deposition numbers COD-ID: 3000289-3000291.

[72]P. S. Salmon, B. G. Aitken, M. Buscemi, H. E. Fischer, L. V. D. Gammond, and A. Zeidler, Structure of magnesium aluminosilicate glass, Institut Laue-Langevin, Grenoble, France, 2018, https://doi.org/10.5291/ILL-DATA.6-05-988.

[73]P. S. Salmon, H. Eckert, H. E. Fischer, L. V. D. Gammond, R. Mendes Da Silva, H. Mohammadi, and A. Zeidler, Structural change in phosphate-based glassy precursors to superionic conducting glass-ceramic electrolytes, Institut Laue-Langevin, Grenoble, France, 2019, https://doi.org/10.5291/ILL-DATA.6-05-1009.

[74]P. S. Salmon, A. Brandon-Bravo, O. de Sousa Costa, A. C. Hannon, A. Zeidler, L. V. D. Gammond, R. Mendes Da Silva, and H. Eckert, Homogeneous nucleation in phosphate-based glassy precursors to fast-ion conducting glass-ceramic electrolytes, STFC ISIS Neutron and Muon Source, UK, 2018, https://doi.org/10.5286/ISIS.E.RB1810217.